Investigation of the electronic and structural phase transitions in $TiSe_2$ and Eu doped $BaTiO_3$

A thesis submitted for the partial fulfillment

for the degree of

Master of Science

as a part of the Integrated PhD. Programme

(Material Science)

By

JANAKY S.

CHEMISTRY AND PHYSICS OF MATERIALS UNIT

JAWAHARLAL NEHRU CENTRE FOR ADVANCED SCIENTIFIC RESEARCH

Bengaluru-560064, INDIA

April 2018

DECLARATION

I hereby declare that the matter embodied in the thesis entitled "**Investigation of the electronic and structural phase transitions in $TiSe_2$ and Eu doped $BaTiO_3$**" is the result of investigations carried out by me at the Chemistry and Physics of Materials Unit, Jawaharlal Nehru Centre for Advanced Scientific Research, Bangalore, India under the supervision of Prof. Chandrabhas Narayana and that it has not been submitted elsewhere for the award of any degree or diploma. In keeping with the general practice in reporting scientific observations, due acknowledgment has been made whenever the work described is based on the findings of other investigators.

_____

JANAKY S.

CERTIFICATE

I hereby certify that the matter embodied in this thesis entitled "**Investigation of the electronic and structural phase transitions in $TiSe_2$ and Eu doped $BaTiO_3$**" has been carried out by Ms. Janaky S. at the Chemistry and Physics of Materials Unit, Jawaharlal Nehru Centre for Advanced Scientific Research, Bangalore, India under my supervision and that it has not been submitted elsewhere for the award of any degree or diploma.

_____

Prof. Chandrabhas Narayana
(Research Supervisor)

ACKNOWLEDGEMENTS

The achievement and final outcome of thesis work required a lot of assistance and support from many people. I am extremely fortunate to have them all around me during my academic life in JNCASR so far. It is always a matter of great pleasure to acknowledge people who have inspired, motivated and supported me by sharing their knowledge and wisdom.

First and foremost I would like to express my deepest gratitude to the Chairman of our unit, my mentor and guide Prof. Chandrabhas Narayana, for his continuous support and guidance. I am extremely thankful to him for his constant motivation, fruitful scientific inputs and enormous freedom in workplace.

I *would like to acknowledge Prof. C. N. R. Rao for being a huge source of inspiration. I feel very fortunate to be able to listen to his inspirational talks.*

I thank all my teachers in JNC, Prof. Balasubrahmanian, Prof. Eswaramoorthy, Prof. Waghmare, Prof. Sundaresan, Prof. Narayan, Prof. Shobhana, Prof. Shivaprasad, Prof.Swapan Pati, Dr. Vidyadhiraja, Dr. Ranjan Dutta, Dr. Shridhar Rajaram, Dr. Rajesh Ganapathy, Dr. Meher Prakash, Dr. Kavita Jain for their valuable coursework and guidance. I would also like to acknowledge our collaborators Dr. Ramanathan Mahendiran, Dr. K.M.Ruby and Dr. Sebastian Peter. It has been a pleasure to work and learn from them. I would like thank present and past Integrated PhD. coordinators, Prof. Eswaramoorthy, Dr. Vidyadhiraja and Prof. Subir.K.Das. Special thanks to Vasu, Anil and Ala Sreenivasa Rao for technical support. I would also like to thank all the admin and support staff of JNC.

I would like to extend a huge gratitude to Rajaji, who has taught me every bit of my work and inspired me to do better everyday. This thesis wouldn't be possible without his help

and support. I would like to thank all my other lab mates Divya, Priyanka, Santanu, Kamali, Prajit, Priyank, Sayan, Amit, Guruprasad and Prince for creating such a wonderful group. It is a pleasure to work with these lovely people. A special token of gratitude to Divya and Rajaji for critical correction of the thesis.

I would also like to thank my classmates and friends in JNC, Niloy, Sukanya, Rajendra, Narendra, Lakshay and Manaswee who have made my time in JNCASR quite enjoyable. I also thank all my friends especially Rosh, Parvathy and Devan for being there always. I thank Sujayammayi for always keeping an extra meal. I thank my father, mother and Madhavan for all the love and encouragement.

PREFACE

This thesis contains results of investigations on the electronic and structural phase transitions in Titanium Selenide and Europium doped Barium titanate samples using Raman spectroscopy as the major tool. The ability of Raman spectroscopy to probe the changes in the electronic and structural properties of a condensed matter system, against the perturbations like pressure, temperature and doping is made use for both the works in this thesis.

It contains the following chapters:

Chapter 1: A thorough introduction to the general aspects of Raman scattering and the fundamental excitations which influences it. Effect of temperature and pressure on materials is also discussed.

Chapter 2: The experimental details which including the design and working principle of Raman setup and the methods of doing high pressure experiments.

Chapter 3: High pressure Raman spectroscopic study of transition metal dichalcogenide, $TiSe_2$ to explore the predicted topological quantum phase transitions.

Chapter 4: Ambient and temperature dependent study of Eu doped $BaTiO_3$ to examine the structural origins of ferroelectricity. The microscopic changes with respect to Nb doping is also analyzed.

TABLE OF CONTENTS

Chapter 1

Introduction

When the light interacts with matter, various phenomena, such as absorption, reflection, transmission, refraction, scattering and so on occur according to the crystal structure and properties of the materials. The study of interaction of light with the materials helps to perceive important information about the electronic and structural properties. Spectroscopy is the technique which makes use of the interactions of electromagnetic radiation with matter, to determine the chemical and physical nature of the material under study. The intensity of the output radiation as a function of wavelength, frequency, or energy is called the "spectrum" hence the name "Spectroscopy" [1].

Absorption spectroscopy is a method which measures the absorption at selected wavelengths when a beam of electromagnetic radiation passes through a sample. While most part of the spectra pass through the sample without much loss in intensity, the radiation's intensity is attenuated at certain wavelengths that has energy equivalent to the energy gap between the ground state and an excited state (electronic, vibrational, nuclear, spin etc.) of the molecule. This method is used for understanding different energy levels of various materials and makes use of all parts of the electromagnetic spectrum. However, scattering is also made use in spectroscopic techniques for the identification and analysis of materials, a major example of which is the Raman spectroscopy. This technique, based on the concept of Raman scattering is a powerful analytical tool that can provide detailed and specific information at the molecular level.

1.1 Raman scattering

The scattering process that induces distortion only in the electron cloud having a negligible mass, so that photons are scattered without any change in frequency is regarded as elastic scattering. It is the predominant scattering process and is called the Rayleigh

scattering [2]. In Rayleigh scattering the energy and wavelength of the incident and scattered light are unchanged. Almost all the light we actually see has scattered between its source and our retina (including the most common example; the blue color of the sky) and that scattering is nothing but Rayleigh scattering. However, the energy change that we can see in vibrational spectroscopy is bound to induce nuclear motion. There is an energy transfer either to the molecule from the incident photon or from the molecule to the scattered photon if the nuclear motion is induced during scattering. Thus the process is inelastic and the energy or wavelength of the scattered light is altered from that of the incident light by one vibration energy unit. This is Raman scattering. It is a weak process as only one in every 10^6–10^8 photons which scatter is Raman scattered. It is one of the most commonly used inelastic light scattering techniques (all inelastic scattering is not Raman scattering).

Raman effect was first proposed by Smekal in 1923 in a theoretical paper that described the inelastic scattering by a system which has two quantized energy levels [3] and the experimental verification for the scattering of light with a change of frequency was given by C. V. Raman in 1928 [4-6]. It lingered practically incompetent because of low sensitivity (being a weak phenomenon) and troubles of overcoming fluorescence from samples for a long time. However, Raman spectroscopy has been revived in the last few decades due to the emergence of extremely sensitive detection devices, efficient filters for filtering Rayleigh scattered light, and lasers as light sources [7]. The versatility of this method which offers an understanding of extremely different fields including, pharmaceuticals, life sciences, geology, mineralogy etc. can downplay the possibilities of other spectroscopic methods [8].

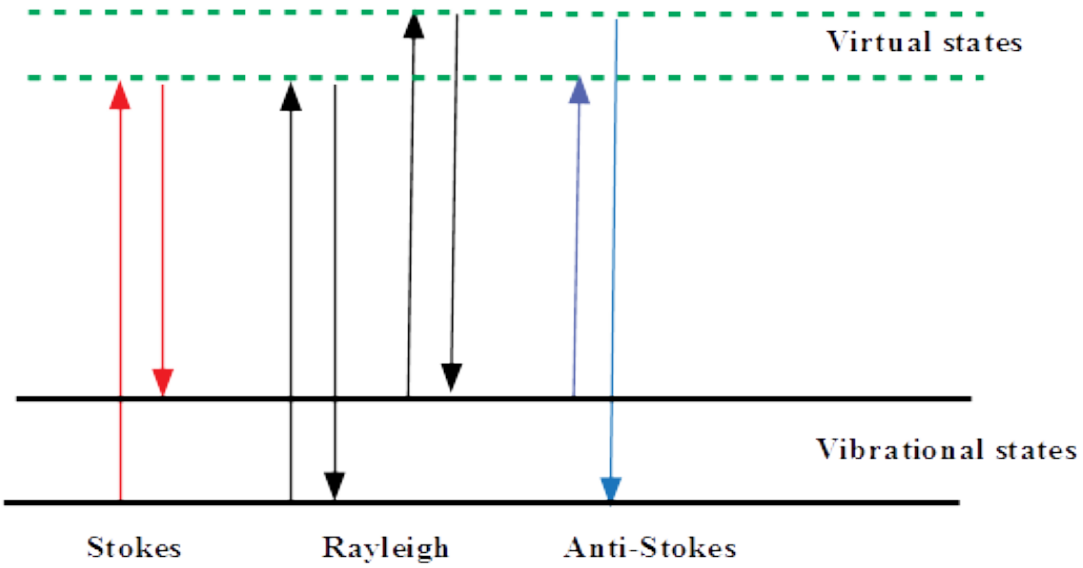

Figure 1.1. Schematic diagram of the Rayleigh and Raman scattering processes.

Figure 1.1 shows the basic processes associated with molecular vibrations. The higher energy states to which the molecule gets excited during scattering are the virtual states. The interaction of the laser with the electrons brings about polarization and forms virtual states. The energy of these states is based on the frequency of the incident light. The Rayleigh scattering that does not involve any energy change is the most intense scattering process. The Raman scattering process along with an absorption of energy by the molecule and its advancement from the ground state to a higher energy vibration state is called Stokes Raman scattering. Whereas, the increase in the energy of the scattered photons due to the transfer of energy from the molecule, when the molecule in the excited state (due to thermal energy) comes back to its ground state is called anti-Stokes scattering. The relative intensities of these two scattering processes are not the same but depend upon the ratio of the population of the ground state and excited state. At room temperature, the number of molecules that would be present in the excited vibrational state

will be small compared to the ground state. Thus, anti-Stokes scattering is weak in comparison with the Stokes scattering [2].

1.1.1 Kinematics of light Scattering

For scattering media (with translational symmetry), the conservation of energy and momentum which determines the kinematics of the Raman scattering can be written in terms of the wave vectors and frequencies of the photons and elementary crystal excitations involved in the process. If a photon of momentum $\hbar k_i$ and energy $\hbar\Omega_i$ is interacting with the medium and a scattered photon is formed which has momentum $\hbar k_s$ and energy $\hbar\Omega_s$. Then,

$$\hbar k_i \pm \hbar k_s = \hbar q \tag{1.1}$$

$$\hbar\Omega_i \pm \hbar\Omega_s = \hbar\omega_p \tag{1.2}$$

where $\hbar q$ and $\hbar\omega_p$ are the momentum and energy of the photon which gets transferred to the medium. This energy is in turn used for the creation or annihilation of elementary excitations (quasi-particles) of the matter such as optical phonons, polaritons, magnons, plasmons, and vibrons (in liquids and gases) in the material with frequency ω_p and wave vector q. The magnitude of the scattering wave vector is determined by the scattering geometry which is apparent from the *Figure 1.2*. In a backscattering geometry, $\Theta = 180^0$ (will be discussed in next chapter), the maximum value of q possible (q_{max}) is obtained from Eq. (1.1) as,

$$q_{max} = k_i + k_s \approx 2k_i \tag{1.3}$$

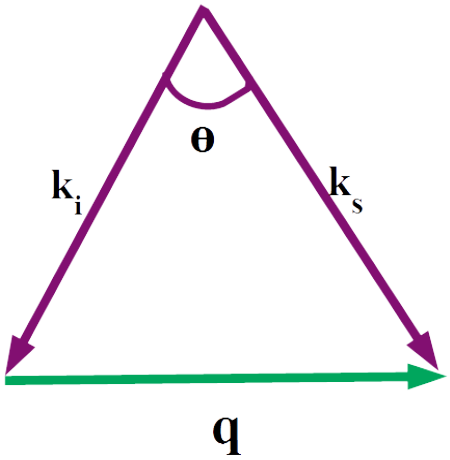

Figure 1.2. *Schematic representation of scattering geometry.*

For visible light, k_i of the order of 10^5 cm^{-1} which is much less than the size of the Brillouin zone (~10^8 cm^{-1}). So, the crystal excitations closest ($q \sim 0$) to the Brillouin zone center i.e., Γ-point are the ones that are being probed in 1st order inelastic light scattering.

1.1.2 Macroscopic theory of Raman scattering

When an electromagnetic wave $E = E_0 e^{i\Omega t}$ interacts with a medium, the nuclei and the electron cloud with opposite charges get spatially distorted and an induced dipole moment P is created. The magnitude of this induced dipole moment is proportional to the electric field. That is

$$P = \alpha E \tag{1.4}$$

where α is the polarizability of the molecule. But for crystals, polarizability has to be substituted with a susceptibility tensor χ_{ij}. This susceptibility gets reformed due to atomic

or lattice vibrations. Since each vibrational mode is a simple harmonic motion in the first approximation, each component in the modified susceptibility can be expanded in Taylor series as

$$\chi_{ij} = (\chi_{ij})_0 + \sum_k \left(\frac{\partial \chi_{ij}}{\partial Q_k}\right)_0 Q_k + \sum_{k,m} \left(\frac{\partial^2 \chi_{ij}}{\partial Q_k \partial Q_m}\right)_0 Q_k Q_m + \text{higher order terms} \quad (1.5)$$

Here, $Q_k = Q_0 \; e^{\pm i\omega_k t}$ is the normal coordinate of the atomic displacements having frequency ω_k (Bloch wave). As the induced polarization can be written as

$$P_i = \chi_{ij} E_{0j} e^{i\Omega t} \quad (1.6)$$

then,

$$P_i = (\chi_{ij})_0 E_{0j} e^{i\Omega t} + \sum_k \left(\frac{\partial \chi_{ij}}{\partial Q_k}\right)_0 Q_0 E_{0j} e^{i(\Omega \pm \omega_k)t} + \sum_{k,m} \left(\frac{\partial^2 \chi_{ij}}{\partial Q_k \partial Q_m}\right)_0 Q_0^2 E_{0j} e^{i(\Omega \pm \omega_k \pm \omega_m)t}$$

$$+ \ldots \text{higher order terms} \quad (1.7)$$

This expression relates the induced polarization to the three oscillating induced dipoles for each normal mode, with frequencies Ω (Rayleigh scattering), $\Omega + \omega_k$ (anti-stokesRaman scattering) and $\Omega - \omega_k$ (Stokes Raman scattering). This explains the formation of Raman peaks symmetrically on both sides of the Rayleigh scattering. In second-order Raman scattering, the scattered photons will have frequencies $\Omega \pm \omega_k \pm \omega_m$. For an oscillating dipole, radiated intensity (I) is proportional to $\left|\frac{d^2 P}{dt^2}\right|$. Thus,

$$I \propto \Omega_i^4 \left(\chi_0^2 E_{0j}^2 + \Omega_s^4 \left(Q_0 E_{0j} \frac{\partial \chi_{ij}}{\partial Q_k} Q_k\right) + \text{higher order terms} \quad (1.8)\right.$$

The first term in the above equation gives the intensity of Rayleigh scattering while the second term corresponds to the intensity of the Raman scattering. For the visible light, the

frequency is ~10^{15} Hz. But the typical phonon frequencies are ~10^{12} Hz which is comparatively much smaller. Thus Ω_i can be approximated to Ω_s so the Raman intensity varies as Ω_i^4.

The partial derivative in the second term of the equation (1.5), $\left(\frac{\partial \chi_{ij}}{\partial Q_k}\right)_0$ is called the "Raman tensor" *R*. For first order Raman process *R* can be expressed by a complex second rank tensor.

$$R = \left(\frac{\partial \chi}{\partial Q}\right)_0 \hat{Q}_0(\omega) \tag{1.9}$$

Where $\hat{Q}_0 = \frac{Q}{|Q|}$; a unit vector parallel to the phonon displacement. Thus, the Raman intensity is given by

$$I_s \propto |\hat{e}_s R \hat{e}_i|^2 \tag{1.10}$$

This explains the dependence of the intensity of the Raman line on the scattering geometry and the symmetry of vibration (scattering cross-section). This also shows that the scattered radiation will be absent for certain polarisation and scattering geometries which in turn constitute the "selection rules of Raman scattering". That is, if a vibration causes a change in polarizability (or susceptibility) such that $\left(\frac{\partial P}{\partial Q_k}\right)_0 \neq 0$ then it is 'Raman active'.

The macroscopic theory which is based on the classical picture of Raman spectroscopy explains the Raman phenomenon without the loss of generality. But it is unable to predict the magnitude and the frequency variations of the susceptibility derivatives. Hence, it is essential to use the quantum mechanical picture to get a better quantitative picture.

1.1.3 Microscopic theory of Raman scattering

The time-dependent third-order perturbation theory can describe the first order Raman process by using quantum mechanics. In the macroscopic theory, a photon is scattered by a phonon, modifying its energy by a discrete value. But, such an interaction is very weak, unless the energy of photon and phonon is comparable. This is not the case for visible or ultraviolet light scattering. Also, the coupling between photons and electrons is very strong. Thus, the microscopic picture is a different approach to understand Raman scattering that involves the excitation of an electron. That is, the interaction between the photons and phonons is mediated by an electron [9]. On the basis of this concept, Raman scattering process by phonons is described including three interactions [10];

1) **Photon-electronic system interaction**: The incident photon excites the electron from its ground state $|i\rangle$ to a virtual state $|f\rangle$ by creating an electron-hole pair.

2) **Electron-phonon or hole-phonon interaction:** The electron or the hole formed interacts with the lattice and due to creation or annihilation of a phonon in the lattice with energy $\hbar\omega$, there is a shift from intermediate state $|f\rangle$ to another state $|f'\rangle$ with lower (Stokes process) or higher (anti-Stokes process) energy than that of the state $|f\rangle$.

3) **Photon emission:** Finally, the electron-hole recombination takes place along with the emission of the scattered photon.

A schematic description of the above process is shown in Fig. 1.3.

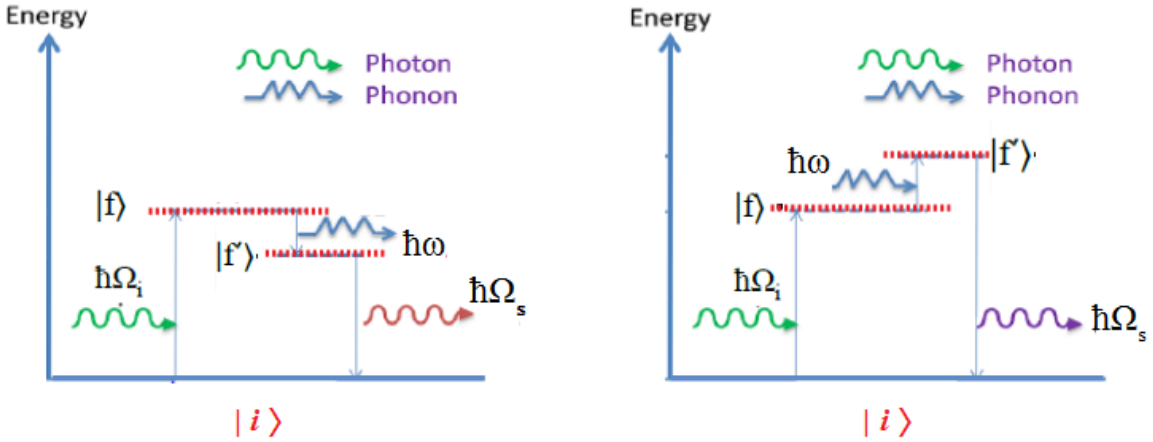

Figure 1.3. Schematic representation of Stokes and anti-Stokes Raman process

Using the combination of the above three process, the scattering cross-section in third-order perturbation theory can be written as [11]

$$|\hat{e}_s R \hat{e}_i| \sim \frac{\langle i|H_{ep}|f\rangle\langle f|H_{eph}|f'\rangle\langle f'|H_{ep}|i\rangle}{(E_f - \hbar\,\Omega_s)(E_{f'} - \hbar\,\Omega_i)} \qquad (1.11)$$

Here H_{ep} represents the Hamiltonian that describes the electron-photon interaction and H_{eph} defines the electron-phonon interaction. E_f, $E_{f'}$, $\hbar\Omega_s$, and $\hbar\Omega_i$ are electronic energy levels as shown in Figure 1.3. For Stokes scattering and anti-Stokes scattering, the differential scattering cross section in terms of the solid angle $d\Theta$ which has a scattering frequency between Ω_s and $\Omega_s + d\Omega_s$ can be written as,

$$\frac{d^2\sigma}{d\theta\, d\,\Omega_s} = vV \frac{\hbar\,\Omega_s^4}{2N\,\Omega_t c^4} |\hat{e}_s . R . \hat{e}_i|^2 (n(\omega)+1)\, g_i(\omega) \qquad (1.12)$$

for Stoke's scattering and

$$\frac{d^2\sigma}{d\theta\, d\Omega_s} = vV\frac{\hbar\,\Omega_s^4}{2N\Omega_t c^4}|\hat{e}_s.R.\hat{e}_i|^2 n(\omega)g_i(\omega) \qquad (1.13)$$

for anti- Stoke's scattering. Here, R is the Raman tensor, υ is the interaction volume, V is the sample volume, N is the number of oscillators in the solid, $g_i(\omega)$ is the spectral line shape response function, mostly taken as Lorentzian and $n(\omega) = \left[e^{\frac{\hbar\omega}{2KT}} - 1\right]^{-1}$ is the Bose-Einstein thermal population factor for phonons. This relation explains the higher intensity of Stokes lines compared to anti-Stokes lines since the excited state is less populated than the ground state.

From the above discussion, it is explicit that there are three major factors that affect the Raman scattering

i. **The incident light frequency, Ω_i:** Since the incident and the scattered light frequency have a very small difference, scattering intensity can be increased by increasing the laser light frequency by a factor of three.

ii. **The scattering volume, V:** The light penetration depth (d) in the material is related to the absorption coefficient (κ) and the wavelength (λ_i) of the incident light by the relation,

$$d = \lambda_i / \kappa \qquad (1.14)$$

Thus penetration depth increases with wavelength and thus increases the scattering volume. But since the reduction in frequency also reduces the intensity drastically, this method is not of any practical advantage.

iii. **Polarization configuration and the crystal symmetry, $\hat{e}_i.R.\hat{e}_s$:** The allowed vibrations in the crystal lattice and their symmetries are determined based on the

components of the Raman tensor (depends on the crystal symmetry) and the specific choice of the polarization. The scattering tensors for different point groups and the appropriate polarization selection rules are listed based on group theory elsewhere [12,13] in great detail.

iv.

1.2 Interactions that affect phonons

It is clear from the above discussion that in condensed matter system, the effect of various perturbations on phonon parameters is what we probe using Raman spectroscopy. The changes in the characteristic of phonons often emerge from interaction with fundamental particles like electrons, atomic spins and even with other phonons. The effect of such interactions become evident from phonon mode parameters like frequency, linewidth, and intensity in the Raman scattering experiments. It is noteworthy to understand that, absorption spectroscopy measurements does not carry this significant information. To explain the effect of temperature on the phonon modes, one has to examine the phonon-phonon interactions (anharmonicity) [14]. In magnetic systems, below the spin-ordering temperature, there will be effects of spin-ordering [15] and the exciting phenomenon like superconductivity from electrical transport measurement can be understood from examining the electron-phonon interactions [16].

1.3 Pressure and temperature effects on materials

Temperature and pressure are the two important independent thermodynamic parameters on which various properties of materials are depended upon. The astonishing

examples of temperature and pressure effects can be seen in nature, in its extremities such as the formation of diamond from graphite to the birth and destruction of stars. Thus the most important and primary purpose of pressure and temperature studies is to get a better understanding of the world around us. In application-based research also, understanding the temperature and pressure dependence of physical properties of materials is very important as it helps to narrow down to the desired properties in the materials and to create an entirely new class of advanced materials such as super-hard materials, superconducting materials etc. Also, such studies are necessary to verify the theoretically predicted, electrical, magnetic, superconducting, and other properties of matter.

Pressure or temperature perturbations can induce both isotropic and anisotropic deformations in crystals, which results in the frequency shifts in Raman spectra. In the study of a material when subjected to the changes in these conditions we can see profound gradual or abrupt changes including phase transitions of many types. In a normal scenario, increase in pressure will affect the equilibrium spacing between the atomic nuclei and there will be a de-localization of electron clouds along with it, thereby distorting the restoring forces. But, increasing the temperature alters the population of the energy levels of each normal modes, and since the energy levels are not equally spaced, the average position of the atoms changes, which can weaken the bonds and result in its disruption and formation of less ordered (higher entropy) structures. Still, pressure variation has much cleaner effect in most materials than the effect of temperature as the pressure effects are changing only a single parameter; volume whereas, temperature affects the phonon population density.

1.3.1 Pressure effects in Raman scattering

The two major changes in the Raman spectra of the materials that are generated by increasing pressure are frequency shift and changes in the Raman line shape. There can also be changes in the selection rules apart from these basic changes, due to pressure-induced structural changes in the materials.

a) Pressure-induced frequency shift: Pressure variation on sample induces changes in the vibrational mode frequencies due to changes in interatomic distances that occurs from the reduction in the lattice volume. This volume dependence of phonon mode frequency can be determined using Gruneisan's law [19]. For α^{th} normal mode, frequency ω_α in a material, the isotropic volume change can be written as,

$$\frac{\partial V}{V} = -\gamma_\alpha \frac{\partial \omega_\alpha}{\omega_\alpha} \tag{1.15}$$

or,

$$\gamma_\alpha = \frac{-\partial \ln(\omega_\alpha)}{\partial \ln(V)} \tag{1.16}$$

where γ_α is the Grunesian parameter. For a material of isothermal volume compressibility β, the Grunesian parameter is given by,

$$\gamma_\alpha = \frac{-1}{\beta} \frac{\partial \ln(\omega_\alpha)}{\partial P} \tag{1.17}$$

But this law can predict the effects of phonon frequency well only when volume change is isotropic. This happens only in covalently bonded 3D crystals. It breaks down in molecular crystals and ionic compounds.

(b) Pressure-induced Raman lineshape changes: In general, Raman lineshape will be varied if the lifetimes of the phonons are altered. But, as pressure changes only the volume, it doesn't have a direct effect on the lifetime of the phonons. However, indirectly, the volume change can affect specific interactions between excitations existing in the material. The lifetime of phonons is inversely proportional to the Raman peak width. Thus, Raman linewidth is an important parameter to monitor the anharmonic interactions amongst phonons.

1.4. Bibliography

1. D. Freude, *Spectroscopy* (University at Leipzeg, 2006)
2. W.E. Smith and G. Dent, *Modern Raman Spectroscopy – A Practical Approach* (John Wiley & Sons, Inc., United States of America, 2005)
3. A. Smekal, Die Naturwissenschaften, *Springer. Nature.* **11**, 873 (1923).
4. C. V. Raman and K. S. Krishnan, *Nature* **121,** 501 (1928).
5. C. V. Raman, *Nature* **121,** 619 (1928).
6. C. V. Raman, *Indian J. Phys.* **2,** 387 (1928).
7. G. D. Pitt, D. N. Batchelder et. al, *IEE Proc.Sci.Meas. Technol*, **6**,152 (2006).
8. M. Schmitt and J. Popp, *Journal of Raman Spectroscopy*, **20**, 37 (2006).
9. R. Loudon, *Advances in Physics*, **50,** 813 (2001).
10. A. S. Barker and R. Loudon, *Reviews of Modern* Physics, **44,** 18 (1972).

11. M. Cardona, *Light scattering in solids I: Introductory concepts, Topics in Applied Physics* (Springer-, New York 1982).
12. D. W. Feldman, J.H. Parker, W. J. Choyke, and L. Patrick, *Phys. Rev.*, **170**, 698 (1968).
13. D. W. Feldman, J. H. Parker, W. J. Choyke, and L. Patrick, *Phys. Rev.*, **173**,787 (1968).
14. R A Cowley, *Proc. Phys. Soc.,* **84,** 281 (1964)
15. R. S. Krishnan, *Proc. Indian Acad. Sci*., **24**, 45 (1946).
16. E. Anastassakis, H. C. Hwang, and C. H. Perry, *Phys. Rev. B,* **4**, 2493 (1971).
17. N. W. Ashcroft, N. D. Mermin, *Solid state physics*, (Cengage learning, India 1976).
18. E.Granado, A. Garcia, et al., *Phys. Rev. B*, **60**, 11879 (1999).
19. M. Blackman, *Proc. Phys. Soc. B*, **70**, 827 (1957).

Chapter 2

Experimental Methods

Raman scattering is a relatively weak phenomenon. Hence, it is difficult to obtain a good signal against the intense background. But, after the discovery of laser, modern monochromators and charge coupled device (CCD) as the detector, Raman spectroscopy has become rather easier [1]. Raman spectrometers are regularly used for characterisation purpose. We have used two different Raman spectrometers for the experiments in this thesis. One of those is a custom- built spectrometer [2,3] and the other one is the commercial spectrometer from HORIBA [4]. Both the spectrometers are described below. A cryo-stage and diamond anvil cell are used for temperature and pressure dependent Raman studies respectively along with these spectrometers to study the effect of these thermodynamic parameters on different materials.

2.1 Custom-built Raman spectrometer

The custom-build micro-Raman spectrometer is equipped with a linearly polarised 532nm line of frequency-doubled Nd:YAG solid state laser (Model GDLM-5015L, Photop suwetech Inc., China) acting as the excitation source with an output power of ~ 15 mW. The schematic of the spectrometer is given in Figure 2.1. Plasma filter (PF;LL01-633-12.5, Semrock) filters the plasma lines present in the monochromatic laser line and the changable neutral density filter (NDF) controls the power of the laser light that falls on the sample (to prevent light-induced chemical or structural changes of the sample). These filters of different transmittance values (75%, 50%, 20% and 10%) can be kept in and out of the beam path according to the intensity requirements. The laser light then falls on to a dichroic mirror (DM) /special mirror (SM; Silver coated only at the centre with 2-3 mm diameter) at an angle of 45^{o} to the surface of the mirror (fabricated by Acexon

technologies, Singapore) which is reflected and directed to the sample via an infinity corrected microscope objective lens (OL) of choice. The sample kept on the micro-stage is focused looking through the eyepiece after inserting the movable mirror (M1) into the light path. The Rayleigh scattered light together with the Raman scattered signals from the sample are collected by the objective lens at backscattering geometry (180^0) and directed onto an edge filter (EF) (LP03-532RS-25, Semrock). Edge filter rejects most the Rayleigh light as well as anti-Stokes Raman signal and lets only the Stokes Raman scattered light to pass. The sample stage is not directly connected to the microscope. So the area under the objective lens is absolutely free for use of different types of experimental setup and hence is open for different kinds of Raman experiments.

The light is then directed using an optical fibre (200 μm multimode single core optical fiber) with band pass of 400-1000 nm using an objective lens and focused on to the 550 mm focal length monochromator (Jobin-Yovn,Triax 550, Instruments SA, Inc., NJ, USA) through a slit of variable width (200μm usually). The objective chosen for most of the experiments is an infinity corrected 50X magnification objective with numerical aperture 0.45mm (NA) and working distance (WD) of 17 mm. (NIKON, L Plan 50X, 0.45 NA, WD 17mm). The revolving sextuple nosepiece adds an option for accommodating six objective lenses and the choice can be made depending on the experimental requirement (depth of focus, working distance, scattering efficiency etc). Light from the monochromator is then dispersed onto the nitrogen cooled CCD (Spectrum one) using a grating via a shutter. The monochromator includes holographic grating of 1800 grooves/mm and blazed reflection type gratings of 1200 grooves/mm (500 nm blaze) and 900 grooves/mm (450 nm blaze). One can choose the grating for optimum resolution and desired spectral range. The CCD consists of a rectangular two-dimensional array of pixels (1024 x 128). Incident light gets

into the monochromator. Labspec software is used to oversee the data acquisition and to control the slit width, spectral range, acquisition time etc. The system has to be calibrated using a silicon wafer before starting any experiment.

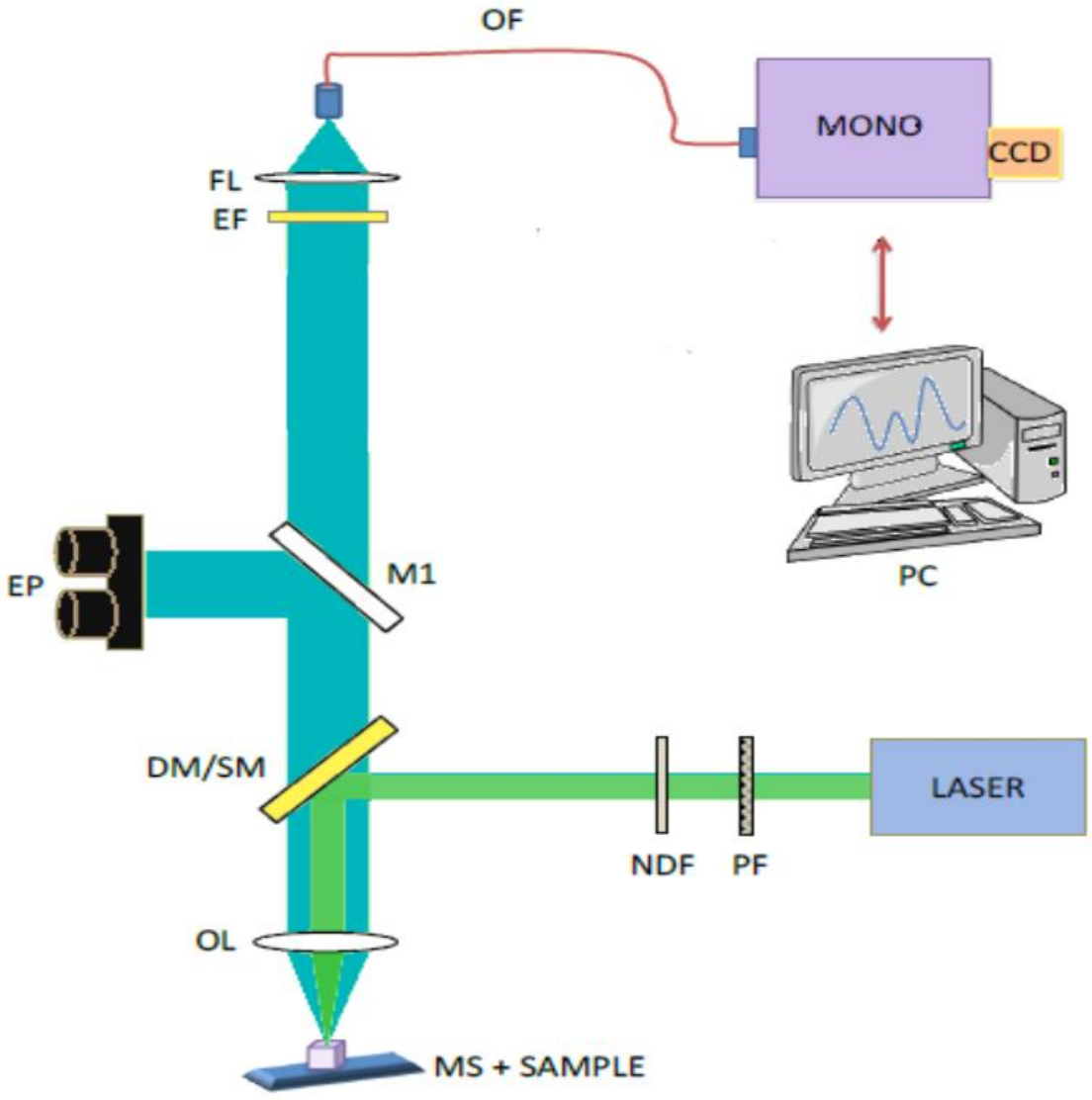

Figure 2.1. Schematic of the micro- Raman spectrometer. MS- Micro stage; OLObjective lens, DM -Dichroic mirror, SM- special mirror, NDF - Neutral density filter, PF - Plasma filter, M1- Movable mirror, EP - Eyepiece, EF- Edge filter, FL- Focusing lens, OF-Optical fibre, MONO – Monochromator, CCD - Charge coupled device, PC – personal computer.

2.2 LabRAM HR Evolution

We also used LabRAM HR Evolution, HORIBA with four different solid-state lasers 532nm (100mW), 633nm (17mW), 405nm (40mW) and 785nm (100mW). The laser can be chosen conveniently according to the requirement and the sample. This is of great use for samples having fluorescence in certain region of the spectra. It is equipped with three gratings 600, 1200 and 1800 grooves/mm. It includes an open electrode CCD, air-cooled to -60^0C. A joystick facilitates the micromotion of the XY stage. The objective can be moved in the Z direction, to focus the laser on the sample, while observing it on the computer through an optical camera. It is a fully automated spectrometer design connected to Labspec 6 software. For high- pressure experiments, this sample stage is removed and an external stage with X and Y movements is connected.

2.3 High-pressure technique

External pressure is a thermodynamic parameter which can be applied on the materials for tuning their properties. This has been discussed in Chapter 1.The pressure generation technique is based on the simple definition of pressure

$$P = F/A \tag{2.1}$$

where F is the force applied to an area A where pressure is applied. Thus a very high pressure can be obtained by employing a large force on a very small area. Thus instead of increasing the force acting, the effective area between the flat faces of anvils is reduced to

reach higher pressures for the experiments in which very small amount of sample is required like Raman, XRD etc. This is the basis of the diamond anvil cell (DAC) in which diamonds with smaller faces are used [5-7].

2.3.1 Diamond anvil cell

The diamond anvil cell (DAC) is the most popular ultra-high-pressure device which is being used by experimentalists to understand many ultra-high-pressure phenomena in materials. This is the most widely known high-pressure research equipment today among all the anvil cells, as diamond is the hardest and least compressible material and is transparent to the most part of the electromagnetic spectrum from X-ray to ultraviolet region. Thus DAC granted the first opportunity to monitor the effects of pressure visually, and it helped to get access to many kinds of experimental techniques, like x-ray diffraction, Raman spectroscopy, and other Optical spectroscopy techniques [8,9]

In DAC, the sample is placed in a small hole made in a metal gasket between the polished parallel faces (culets) of two opposed diamond anvils and is subjected to pressure when a force pushes the two opposed anvils together. In this way, only a small force is enough to create extremely large pressures in the sample chamber. Figure 2.2 shows the diagram of a simple DAC. There are five types of DAC, which has differences in the ways of generation of force and the anvil-alignment mechanisms [10-14]. They are,

i.NBS cell

ii.Basset t cell

iii.Mao-Bell cell

iv.Syassen-Holzapfel cell

v.Merrill-Bassett cell

We have used the Mao-Bell cell for the experiments in this thesis.

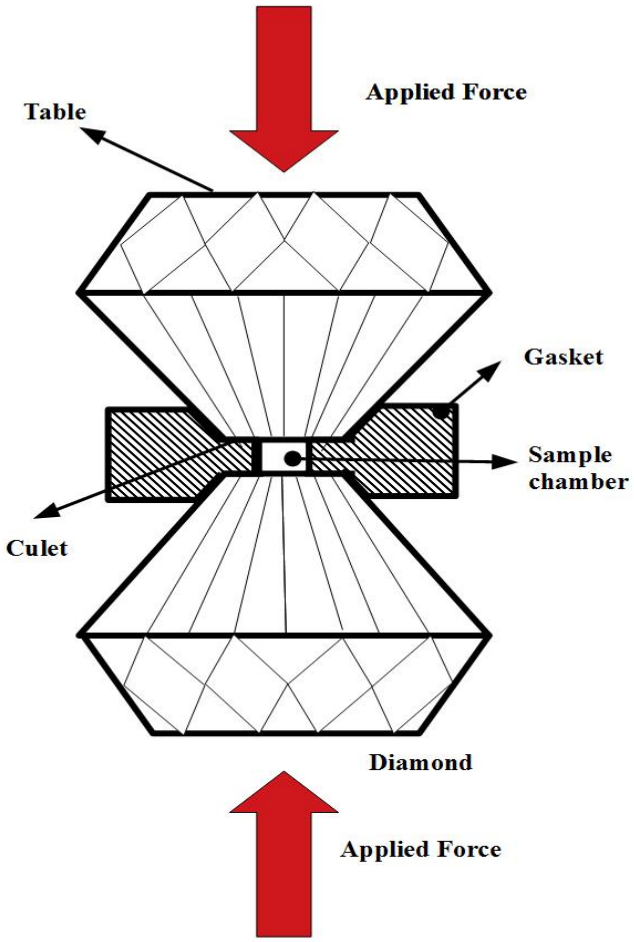

Figure 2.2. Schematic diagram of diamond anvil cell

2.3.2 Mao-Bell Cell

The Mao-Bell cell was developed by Mao and Bell at the Geophysical Laboratory in Washington for pressures beyond a mega-bar [11]. The photograph of cell used for the experiment in this thesis is shown in Fig 2.3. On the right side an exposed view of the DAC. The generation of pressure in a DAC is based on the principle of massive support. The sample placed in a hole [100-250 μm] made in a Stainless steel (SS) gasket between the culets of diamond called the sample chamber, is positioned at the center of the gasket. Mechanical load is applied to the rockers on which the diamond sits by Bellville spring-loaded lever arm mechanism [15]. A pressure transmitting medium (Methanol:Ethanol mixture) and pressure calibrant (Ruby) are loaded along with the sample in the sample

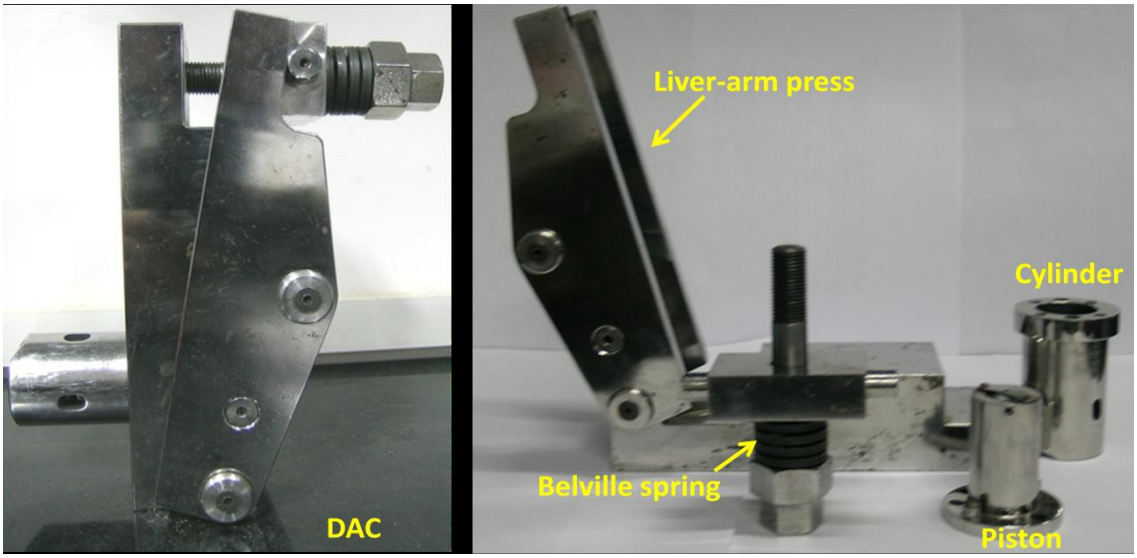

Figure 2.3. Photograph of the DAC used (left) and an exploded view of the DAC (right)

chamber for high-pressure experiments. The more generously proportioned body and the lever-arm system facilitate generation of larger force, and the long piston-cylinder

assembly combined with the tungsten carbide mounts ensures excellent alignment of the diamonds.

2.3.3 Diamonds and alignment

The four most critical things to be noted for the diamonds used in an anvil cell are cut, color, clarity, and carat. Gem quality, brilliant cut diamond stones are the ones used as anvils. Diamonds containing Nitrogen platelet impurity (type I) is commonly used, even though it has a very strong absorption in the mid-IR region since the purest type II diamond which is transparent to all electromagnetic radiation is rare and expensive. The size of the diamond may vary from 1/2 carat to 1/8 carat and is chosen depending on the requirement. In general, larger diamonds are preferred for higher pressures. Still, culet size is the major factor that determines the pressure that can be achieved using the diamonds. A formula that can be used to calculate the maximum attainable pressure (P_{max}) that can be achieved using a diamond anvil with culet diameter *d,* is given by [16]

$$P_{max} = 12.5/(d\ (\text{mm}))^2 \tag{2.2}$$

Also, the culet should be much smaller compared to the table of the anvil to intensify the low pressure applied to the table into a high-pressure at the culet. The ratio of the table area to the culet area gives the pressure intensification [17].

A very critical factor of the experiment is the accurate alignment of the two diamond culets. These two stressed surfaces must be laterally and parallelly aligned with each other to avoid severe gasket deformity and breaking of the diamonds. The first step of alignment is to ensure the lateral alignment of diamond anvils to locate one of the culets

precisely above the other by translation of the rockers along the X and Y axes. The piston is inserted into the cylinder and kept on a V-block, to view the culets (very close to each other, but not touched) in perpendicular directions through the hole on four sides of the cylinder under the optical microscope. The the set of screws are adjusted through the ports in the cylinder wall until the culets are aligned in the X-Y direction. The final part is the angular alignment which is done by the light fringe technique (Newton's ring). For this, the culets that are laterally aligned are made to touch each other slowly and the interference pattern formed is observed through the cylinder from the top under the microscope. If color fringes or dark striations are present, the culets are not parallel and hence the Allen head screws on the top of the cylinder are adjusted until only a single dark/bright fringe is present which in turn confirms that they are parallel (zero fringes for perfect alignment).

2.3.4 Gaskets

As Jayaraman tells in his review about the diamond anvil cells [8], "The introduction of the gasket into the diamond anvil apparatus is a very important development in the history of the DAC, for it is this discovery which paved the way to make the DAC into a quantitative tool for high-pressure research." The gasket provides hydrostatic pressure formation in the sample chamber which is filled with pressure-transmitting medium. In addition to that, gasket also supports the culets by forming a ring around the diamonds on compression. The diagram of a drilled gasket with sample chamber used for high-pressure experiments is shown in Figure 2.4.

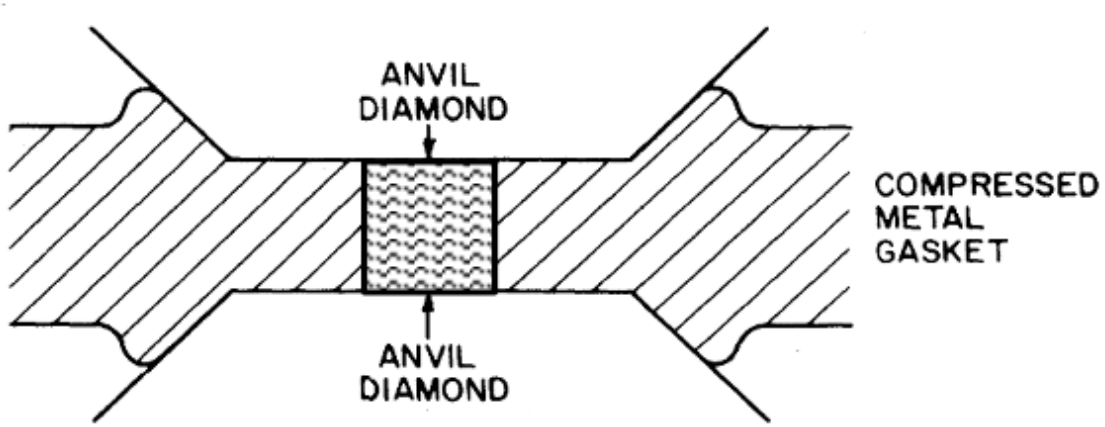

Figure 2.4. Schematic diagram of intended gasket

The gasket is introduced between the culets of two opposed diamonds and is compressed to reduce the thickness of the gasket (pre-indentation) before pressurization. Pre-intendation is important for hardening the gasket and reducing the deformation of the hole. A hole is drilled at the center of this pre-intended area which acts as the sample chamber in which sample and the pressure calibrant is kept and filled with the pressure transmitting medium. For gaskets of small thickness, the size of the hole reduces when pressure is increased since the inward destabilizing force is higher than the outward stabilizing force. On the other hand, elongation of the gasket happens for thicker gaskets. Thus the stability of the gasket can be monitored by observing the effect of these two equal and opposite forces acting between the gasket and the culet surface. Hence it is crucial to observe the changes happening in the shape of the gasket hole and the experiment has to be stopped in case of asymmetric elongation or extreme contraction.

Stainless steel gaskets (T301) of the initial thickness of ~250 μm has been used which is pre-indented to a thickness of 60 μm before drilling. Using a micro drill equipment with a miniature solid carbide drill bit, a hole is drilled at the center of the pre-indented area. The gasket was fixed on the rocker using an adhesive for inhibiting its movement for pressurization.

2.3.5 Pressure transmitting medium

The sample has to be surrounded by a pressure transmitting medium (PTM) inside the sample chamber to bring about hydrostatic pressure conditions [18]. The critical criteria of the PTM of choice are; i) it should not react with the sample and ii) should stay hydrostatic in the required pressure range. For example [18-20] the hydrostatic limit of silicone is up to ~ 2 GPa, isopropyl alcohol ~ 4 GPa, water ~ 5 GPa, methanol ~ 8GPa, 4: 1 methanol to ethanol ~ 10 GPa, 16:3:1 methanol to ethanol to water ~ 14.5 GPa. These liquids become quasi-hydrostatic above the mentioned pressure due to solidification. Solid media like NaCl (~ 7 GPa,) silver iodide (~ 7GPa) can also be used. Noble gases like He and Ne can be used for very high pressures within the hydrostatic range till ~70GPa and ~16GPa respectively. For the experiments in this thesis, we have used 4:1 methanol to ethanol solution as PTM.

2.3.6 Pressure measurement

In the high-pressure experiments using DAC, ruby fluorescence method is the most commonly used pressure calibration technique [21]. Ruby (5% Cr^{3+}- doped Al_2O_3) is a

well suited in-situ pressure sensing material in high-pressure work because of its two high intense sharp luminescence peaks (R1, R2) shown in Figure 2.5 which exhibit pressure dependence. Crystal field splitting of d-orbitals of Cr^{3+} ion surrounded by the oxygen atoms in an octahedral geometry is the origin of these lines which occur at ~ 694.2 nm (R1) and 692.7 nm (R2). Under static high pressure, the shift in the wavelength of R1 line is generally used for pressure calibration [22]. The two lines shift equally and the separation between them remains constant under hydrostatic conditions. This can be expressed as [23]

$$P(GPa)= \frac{1904}{B} \left[\left(1+\frac{\Delta\lambda}{\lambda_0}\right)^{B}-1\right] \quad (2.3)$$

where $\Delta\lambda= \lambda_P - \lambda_0$, is the wavelength difference at pressure P and ambient pressure. The value of the constant B= 7.665 and 5 for quasi-hydrostatic and non-hydrostatic conditions respectively. The peaks broaden for non-hydrostatic conditions. For the high-pressure experiments in this thesis, the ruby fluorescence method has been used for calibration.

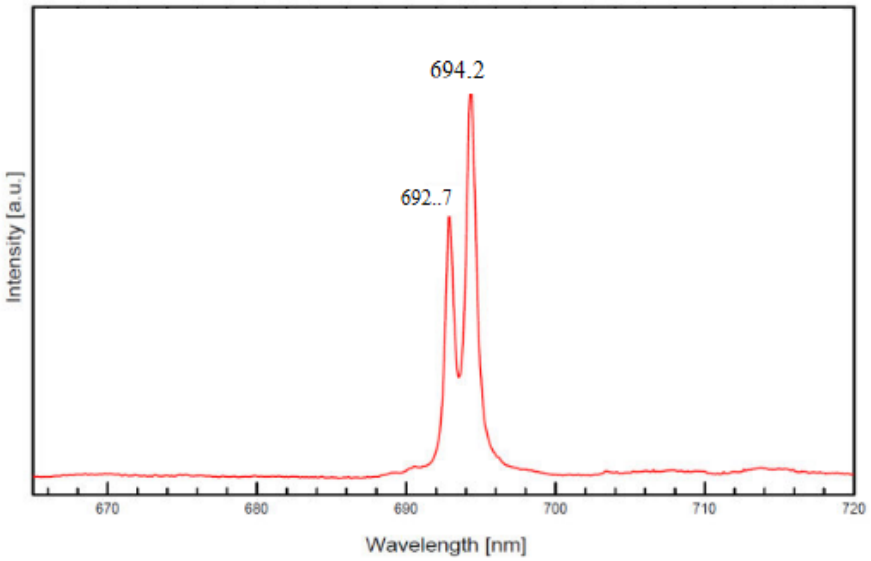

Figure 2.5. Ruby flurescence spectrum with R1 and R2

2.4 Temperature dependent studies

The temperature dependent studies has been done using the cryo-stage (Linkam THMS 600, Linkam Scientific, UK) which has a temperature-controller (Linkam TMS 94) which maintains the set temperature and liquid nitrogen pumping module (LNP 94).Temperature is regulated with an accuracy of ±0.1K. The external control unit also executes the ramping up and down of the temperatures at user specified rates. We have used a ramp rate of 10^{o}/min.

2.5 Bibliography

1. J. Coates, *Appl. Spect. Rev.* **33**, 267 (1998).
2. G. Kavitha, S. R. C. Vivek, A. Govindaraj, and C. Narayana, *Proc. Indian Acad. Sci. Chem. Sci.* **115**, 689 (2003).
3. G. V. P. Kumar and C. Narayana, *Curren. Sci.* **93**, 778 (2007).
4. *LabRAM HR Software and Hardware User Guide*, Horiba, France
5. C. E. Weir, E. R. Lippincott, A. Van Valkenburg, and E. N. Bunting, *J. Res.Natl. Bur. Stand.* **63 A**, 55 (1959).
6. W. A. Bassett, *High Pres. Res.* **29**, CP5 (2009).
7. J. C. Jamieson, A. W. Lawson, and N. D. Nachtrieb, *Rev. Sci. Instrum.* **30**, 1016 (1959).
8. A. Jayaraman, *Rev. Mod. Phys.* **55**, 65 (1983).
9. A. Jayaraman and S. K. Sharma, *Curren. Sci.* **74**, 308 (1998).
10. G. Huber, K. Syassen, and W. B. Holzapfel, *Phys. Rev. B* **15**, 5123 (1977).
11. H. K. Mao and P. M. Bell, *Carnegie Inst. Washington Yearbook* **77**, 904 (1975).

12. G. J. Piermarini and S. Block, *Rev. Sci. Instrum.* **46**, 973 (1975).

13. L. Merrill and W. A. Bassett, *Rev. Sci. Instrum.* **45**, 290 (1974).

14. D. J. Dunstan and I. L. Spain, *J. Phys. E: Sci. Instrum.* **22,** 913 (1989).

15. H. K. Mao and P. M. Bell, *Rev. Sci. Instrum.* **8**,50 (1979)

16. D. J. Dunstan and I. L. Spain, *J. Phy. E: Sci. Instrum.* **22,** 913 (1989).

17. T. Blachowicz, R. Bukowski, and Z. Kleszczewski, *Rev. Sci. Instrum.* **67,** 4057 (1996).

18. S. J. You, L. C. Chen, and C. Q. Jin, *Chi. Phy. Lett.* **26,** (2009).

19. J. H. Weaver et. al. *Phys. Rev. Lett.* **66**, 1741 (1991).

20. G. J. Piermarini, S. Block, and J. D. Barrnett, *J. Appl. Phys.* **44**, 5377 (1973).

21. J. D. Barnett, S. Block, and G. J. Piermarini, *Rev. Sci. Instrum.* **44**, 1 (1973).

22. K. Syassen, *High Pressure Research* **28,** 75 (2008).

23. H. K. Mao, P. M. Bell, J. W. Shaner, and D. J. Steinberg, *J. Appl. Phy.* **49,** 3276 (1978).

Chapter 3

High-Pressure Raman Studies of $TiSe_2$

To execute this problem, we have collaborated with the group of Dr. Sebastian C. Peter for sample preparation.

3.1 Introduction

The topological insulators are a class of materials that are being actively researched in condensed-matter physics in the past few years based on the recent understanding that the spin-orbit interaction can give rise to topological insulating electronic phases [1- 4]. The topological insulators have an energy gap separating the highest occupied electronic band and the lowest empty band similar to the normal insulator. But, in spite of the insulating nature in its bulk, the gapless states are protected by time-reversal symmetry in the boundaries, due to strong spin-orbit coupling (SOC). Thus, the surface or edge states of a topological insulator generate a conducting state which shows exotic properties compared to any other common 1D or 2D electronic systems. The topological classification is given by the so-called topological invariant Z_2 which is 1 for strong (Z_2) topological insulators and is zero, for weak topological or trivial insulators [2]. Besides the fundamental interest, this class of materials have potential applications in spintronics, quantum computing, and thermoelectric energy conversion devices [5].

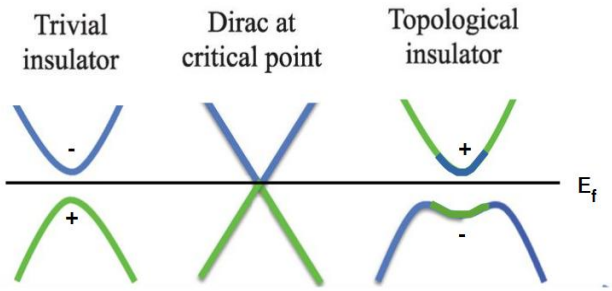

Figure 3.1. *The topological quantum phase transition from a normal insulator to a topological insulator. The "+" and "–" signs denote the even and odd parity of the bands at the time-reversal invariant point, respectively.*

There are few examples of SOC narrow band gap materials, which act as trivial insulators (Z_2= 0) at ambient conditions but are converted as nontrivial topological insulators (Z_2 =1) under the application of strain. This transformation is called the topological quantum phase transition (TQPT) [6-8]. It is a second-order isostructural transition and is the result of an adiabatic band inversion occurring at the time-reversal invariant momenta point (TRIM) with parity change (odd/even). The band inversion diagram of a topological insulator is shown in Figure 3.1. To bring about topological transition, stain can be induced in a system by chemical and physical methods. For example, topological transitions are induced by chemical doping in $TlBi(S_{1-x}Se_x)_2$ and $Pb_{1-x}Sn_xSe$ systems [9,10]. Similarly, TQPT is induced by physical strain (hydrostatic pressure) in BiTeI, BiTeBr, Sb_2Se_3, and 1T-$TiTe_2$ [11-14].Compared to chemical methods, hydrostatic pressure is a cheaner and effective parameter to tune the SOC strengths, hybridization, density, and crystal field splitting in narrow band gap materials which can give rise to TQPT.

3.1.1 Titanium Diselenide

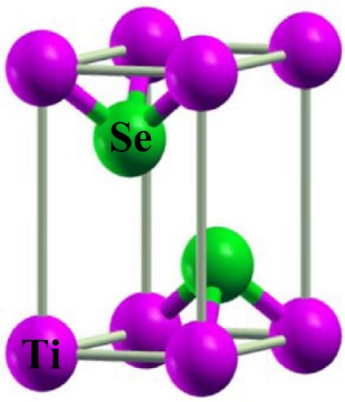

Figure 3.2. Schematic diagram of $TiSe_2$ unit cell.

Titanium diselenide ($TiSe_2$) is a transition metal dichalcogenide (TMD) that belongs to a group of the van der Waals materials characterized by the layered crystalline structures and exhibit charge density wave (CDW) transitions at low temperatures. Generally, Titanium dichalcogenides TiX_2 (X = Se, Te, S) are hexagonal crystal structures in which X-Ti-X slabs with ionic bonding are separated by a van der Waals gap, leading to a quasi two-dimensional nature as shown in Figure 3.3. In each layer, a Ti atom is surrounded by six chalcogen atoms in the octahedral configuration forming either octahedral (2H) or trigonal prismatic (1T) structure. $TiSe_2$ forms 1T ($P\bar{3}m1$) structure which has one Ti and two Se atoms per unit cell as shown in Figure 3.2

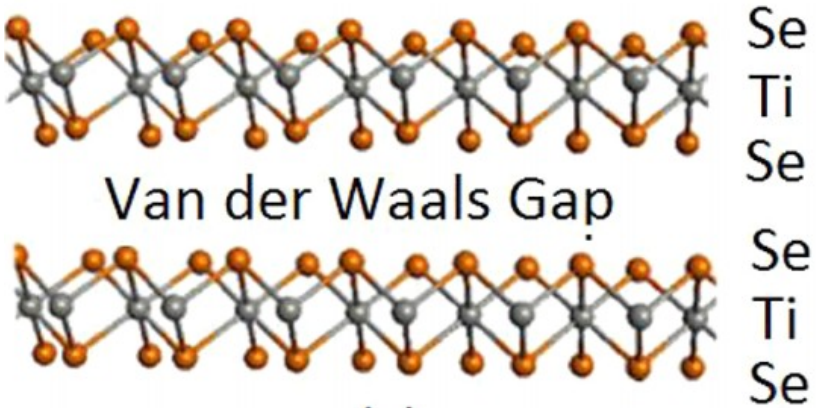

Figure 3.3. Schematic of the layered structure of $TiSe_2$ adapted with permission from Nano Lett. 12,11,5941-5945 . Copyright(2012) American Chemical Society.

3.1.2 Theoretical prediction

Z.Zhu et al. have applied density functional theory to demonstrate a pressure induced trivial-nontrivial-trivial topological phase transition for 1T-$TiSe_2$ [15]. The transition in the 1T-$TiSe_2$ semimetal is ascribed to inversion of Se 4p and Ti 3d bands with

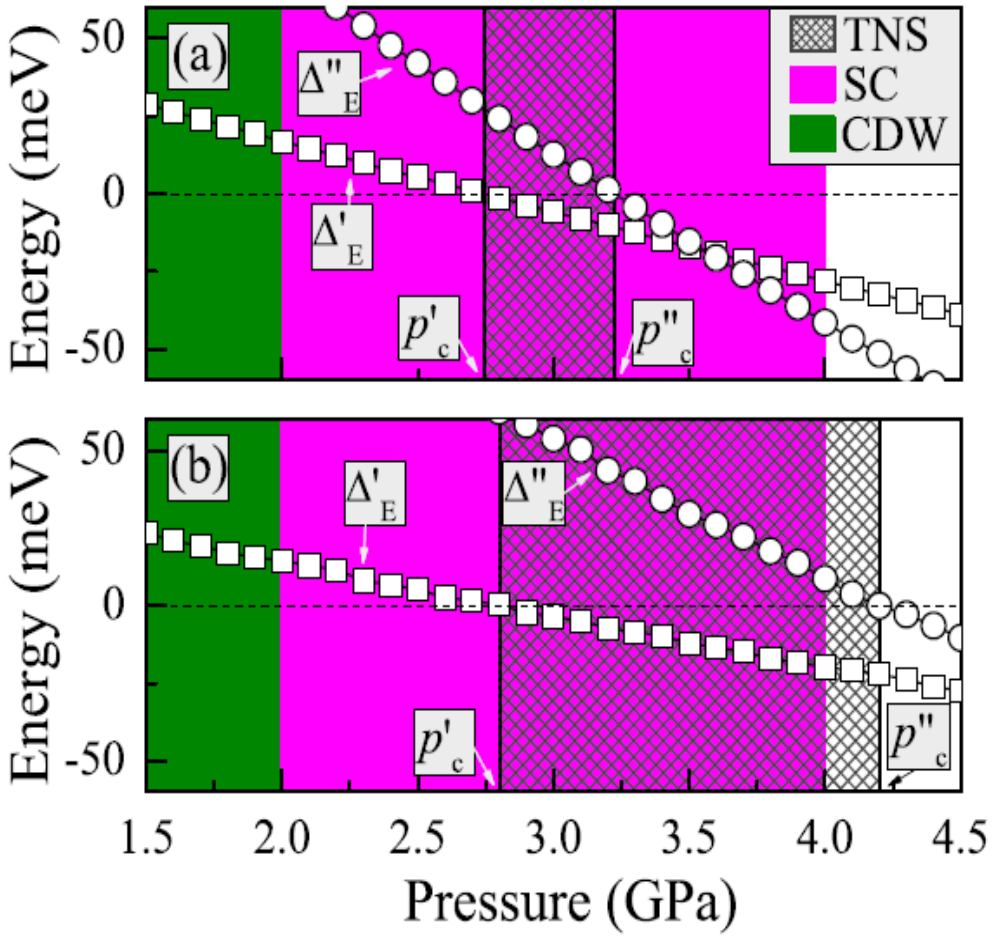

Figure 3.4. Topological phase diagram of the normal state of 1T-TiSe2 under pressure. The white dots show the experimental phase diagram of the ground state. TNS, SC, and CDW denote the topologically nontrivial state, the superconducting ground state, and the charge density wave ground state, respectively. Δ'_E and Δ''_E represent the energy differences of the Γ^-_{56} and Γ^+_4 states and of the Γ^-_4 and Γ^+_{56} states, respectively. (b) Same as (a) but for another set of a/a0, c/c0, and z,Adapted with permission from Scientific Reports 4 , 4025 Copyright (2014) Springer Nature

different parity at the Γ-point. Topological phase diagram of 1T-$TiSe_2$ under pressure is given in Figure 3.4. The critical pressures of the trivial-nontrivial (p'_c) and nontrivial to

trivial (p''_c) transitions for two different sets of a/a_0, c/c_0, and z values are obtained as ~2.7 GPa and ~3.2 GPa, and ~ 2.8 GPa and ~ 4.2 GPa respectively. Also, the green region in the figure is the charge density wave ground state at a pressure below 2 GPa and the pink region from 2GPa to 4GPa is the superconducting ground state (both are low- temperature states). The exciting result is that the pressure range p'_c to p''_c overlaps with the superconducting pressure range. This can lead to self-induced topological surface superconductivity in pressurized 1T-$TiSe_2$.

Interestingly, the prototype system of $TiSe_2$, 1T-$TiTe_2$ was also reported to show similar isostructural electronic transitions at ~2 GPa and ~4 GPa from our group [14] which is supported by the theoretical predictions. $TiSe_2$ is expected to show a similar behavior as anticipated from first principle calculations. This motivates us to do the high-pressure investigation of the 1T-$TiSe_2$ system.

Nontrivial electronic band inversion can be probed directly using Angle-resolved photoemission spectroscopy (ARPES). But ARPES measurements under pressure have not been implemented yet due to the experimental difficulties. However, the indirect evidence of TQPT can be obtained from Raman spectroscopy by monitoring the changes in optical phonon linewidth through the mechanism of electron-phonon coupling.[11-14,16,17] Mathematically, Raman linewidth is directly proportional to the square of the energy-resolved electron-phonon matrix elements [18]. Hence, the full width half maxima (FWHM) of Raman peaks contain information about the dynamics of electron- phonon coupling.

3.2 Experimental details

The 1*T* -TiSe2 was synthesized by mixing 0.1579 g of titanium shots (99.99%, Alfa Aesar) and 0.8420 g of selenium shots (99.99%, AlfaAesar) in a 9 mm diameter quartz tube. The tube was flame-sealed under a vacuum of 10−3 Torr, achieved with the help of a rotary pump, to prevent oxidation during heating. The tube was then placed in a vertically aligned tube furnace and heated to 750°C over a period of 8 h to allow proper homogenization. Subsequently, the temperature was kept constant for 6 days. Finally, the system was allowed to cool to room temperature over a period of 10 h. No reaction with the quartz tube was observed. A red polycrystalline $TiSe_2$ along with a few flakes of single crystal was formed.

Raman scattering measurements were conducted using LabRAM HR Evolution Raman spectrometer (UHTS600) in the backscattering geometry (180°) as explained in chapter two. The spectral resolution is ~1 cm^{-1} for a grating of 1800 lines per mm. The *in-situ* high-pressure Raman spectroscopic measurements of single crystal $TiSe_2$ were performed using the Mao-Bell type diamond anvil cell (DAC) which has diamonds of culet size 400 μm. A T301 stainless steel gasket with the starting thickness ~ 250 μm was pre-indented to a thickness ~ 60 μm. Then a hole of ~150 μm diameter was drilled at the center using tungsten carbide drill bit. This sample chamber has filled with the sample, ruby which acts as the pressure calibrant and a mixture of methanol: ethanol (4:1) which is used as the pressure-transmitting medium (PTM). The pressure is calculated by the ruby fluorescence method. Methanol:ethanol (4:1) medium guarantees hydrostatic limit up to ~10 GPa and quasi-hydrostatic limit up to 25 GPa. The accumulation time of each

spectrum was done for 30 minutes and the laser power was kept ~1 mW to avoid light-induced damage and oxidation of the sample.

3.3 Results and discussion

Based on group theory analysis, IT-$TiSe_2$ ($P\bar{3}m1$) system has nine vibrational modes [19] in its irreducible representation given by,

$$\Gamma = A_{1g} + E_g(2) + 2A_{2u} + 2E_u(2)$$

where gerade (E_g and A_{1g}) and ungerade (E_u and A_{2u}) modes represent the Raman active modes and IR-active phonon modes respectively. Further, A_{1g} mode represents the stretching of two Se atoms in the unit cell along the out of plane direction (atomic vibrations parallel to the *c* axis) whereas the degenerate E_g mode is the symmetric in-plane bending of the Se atoms (along the *ab* plane). The schematic of Raman modes (A_{1g} and E_g) of vibration are shown in Figure 3.5.

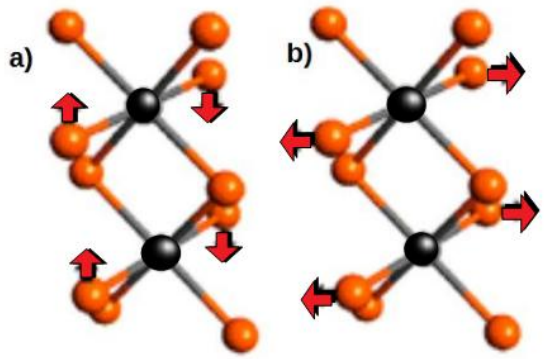

Figure 3.5. Raman modes of $TiSe_2$ a) A_{1g} mode b) E_g mode.

Raman modes were fitted using the Lorentzian line shape function and peak positions were obtained around 135 cm^{-1} and 198 cm^{-1} for the ambient spectrum. Based the existing literature [20], the modes at 135 cm^{-1} and 198 cm^{-1} are assigned to E_g and A_g modes respectively. In addition to that, for polycrystalline samples, we observed a strong peak around 233 cm^{-1}, named the U_1 mode (sometimes double peak around 233 cm^{-1} and 236 cm^{-1} named U_1 and U_2) at ambient conditions. This peak characteristics change according to incident wavelength and power. At the same time, the single crystal only shows the expected modes (E_g and A_g) and does not show much variation in the spectrum with the wavelength that is being used. The Raman spectra of IT-$TiSe_2$ for both polycrystalline and single crystal samples is shown in Figure 3.6.

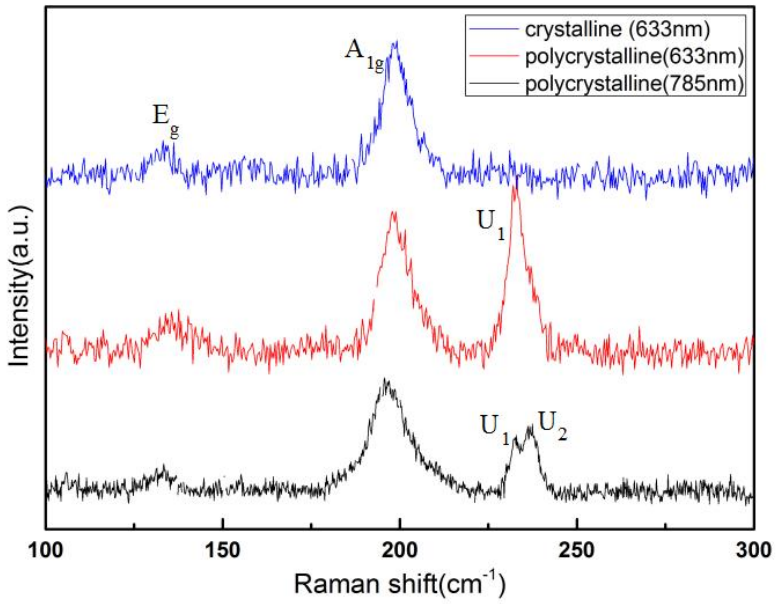

Figure 3.6. Raman spectra of single crystal and polycrystalline samples of $TiSe_2$

The presence of additional peaks can be explained on the basis of selenium migration and agglomeration in $TiSe_2$ [21]. Lioi et al, have reported that selenium is migrated to the surface of the crystal from the bulk and integrate to form islands with a range of dimension from few tens to several hundreds of nanometers under 350K temperature. One can assume that, laser heating can result in the increase of temperature above 350K at a very specific spot. Thus, laser heating can result in the formation of islands of Se. In the literature, Se is reported to have different allotrope and hence can have different the symmetric stretching frequencies according to the crystal structure [22]. The additional peaks seen in the Raman spectra of polycrystalline $TiSe_2$ indicate the presence of trigonal selenium (233 cm^{-1} and 236 cm^{-1}) formed due to laser heating. The absence of these peaks in single crystal $TiSe_2$ spectra is explainable as, the result of decrease in surface area, reducing the surface effects in the single crystal. It was observed that, at a higher laser power Se peaks reappear in the single crystal, confirming the above explanation.

To explore more about the theoretically predicted isostructural transitions, Raman spectroscopy measurement of single crystal $TiSe_2$ was done under pressure up to ~20GPa. The evolutions of the Raman spectra of $TiSe_2$ with pressure up to ~ 15 GPa is shown in Figure 3.7. As evident from the figure, the intensity of both the peaks are (E_g and A_{1g}) are decreasing gradually with the increase of pressure and the E_g mode is getting disappeared ~ 3.5 GPa. Also, the intensity of A_{1g} mode is observed to reduce drastically above ~ 6.0 GPa.

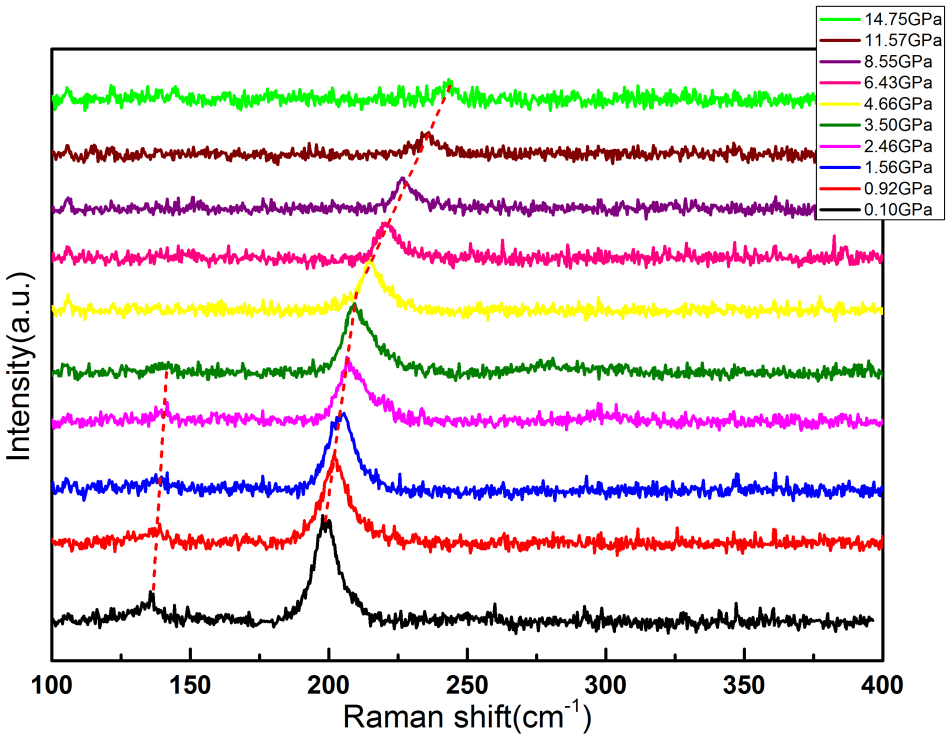

Figure 3.7. Stack plot of $TiSe_2$ Raman spectra with changing pressure.

Figure 3.8 shows the evolution of spectra in the high-pressure region above 10GPa, where there are major changes in the Raman spectra. Two new peaks have emerged at 152cm^{-1} and 187 cm^{-1} (from ~15 GPa) which are named as N_1 and N_2 for convenience. Also, there is a drastic reduction of the intensity of A_{1g} mode with the increase of pressure. This along with the appearance of the new peaks is a clear indication of a structural phase transition. The spectrum after depressurization was identical to the ambient spectra, which suggests that the observed changes are reversible.

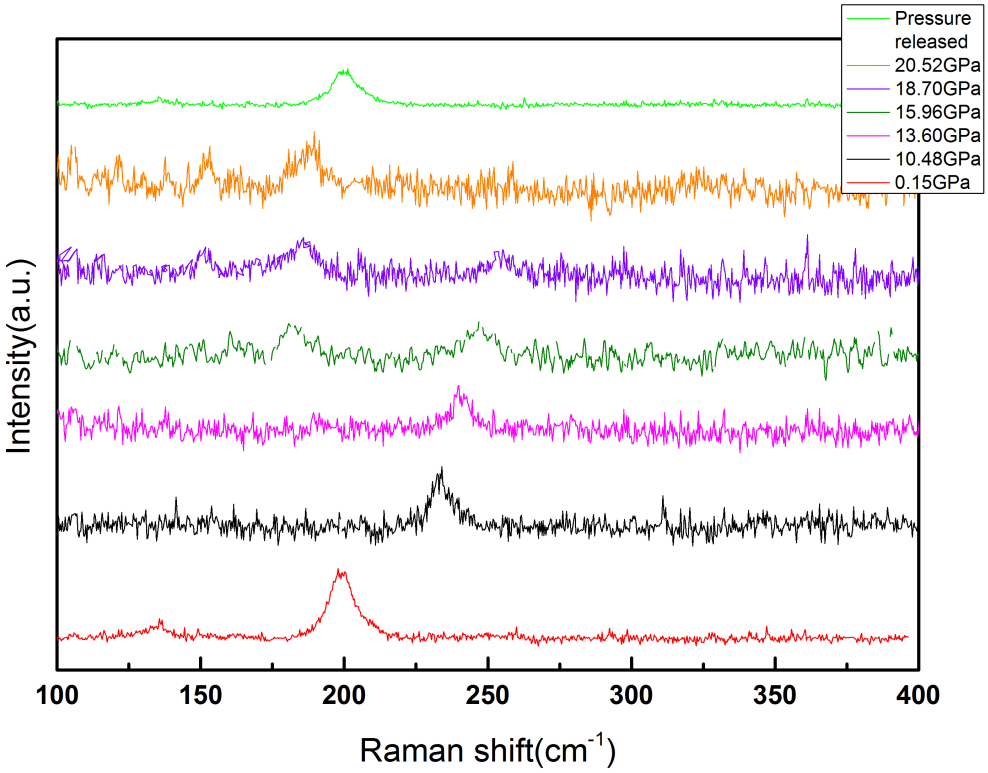

Figure 3.8. Stack plot of Raman spectra of $TiSe_2$ above 10GPa

To get a better understanding of the evolution of Raman spectra with pressurization, Raman mode frequencies and peak width are plotted against pressure as shown in Figure 3.9. In general, the phonon modes are expected to harden (blueshift) during the hydrostatic lattice compression. It is evident that there is a blue shift in all the modes (E_g, A_{1g}, N_1, and N_2) with pressure. There are two noticeable anomalies in the frequency of A_{1g} mode around 6 GPa and 11 GPa. These characteristics are confirmed by repeated experiments and analysis. The 11 GPa anomaly can represent a structural phase transition similar to the reported structural phase transition in $TiTe_2$ [14]. The appearance of new Raman modes ~15.96 GPa (N_1 mode) and ~18.70 GPa (N_2 mode) confirms the structural phase transition and the presence of the A_{1g} mode at higher pressures indicates

phase coexistence (mixed phase). There is an other anomaly in the slope of A_{1g} mode Raman frequency ~ 6 GPa which is an isostructural transition.

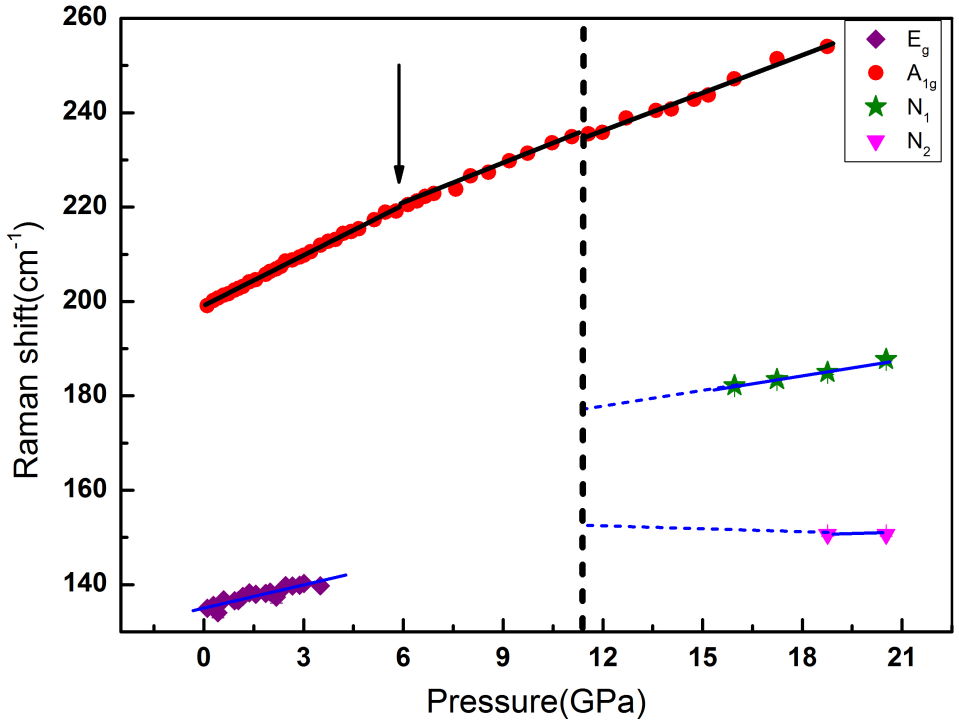

Figure 3.9. Pressure versus Raman shift of phonon modes (A_{1g}, Eg, N_1 and N_2) of TiSe2. The solid lines is a guide to the eye.

Raman linewidth studies can impart information about the phonon-phonon interactions and the excitation-phonon interactions in a system [23-26,14]. In that regard, Raman line width of A_{1g} mode with respect to pressure is plotted. The change in FWHM of A_{1g} mode (Lorentzian peak fitted) with respect to increasing pressure is shown in Figure 3.10. It has to be made clear that the hydrostatic limit of methanol: ethanol (4:1) mixture (PTM) bounds the accuracy of information about the linewidth of any sample till ~10GPa [27]. Hence the plot shows only the linewidth analyzed up to 10 GPa.

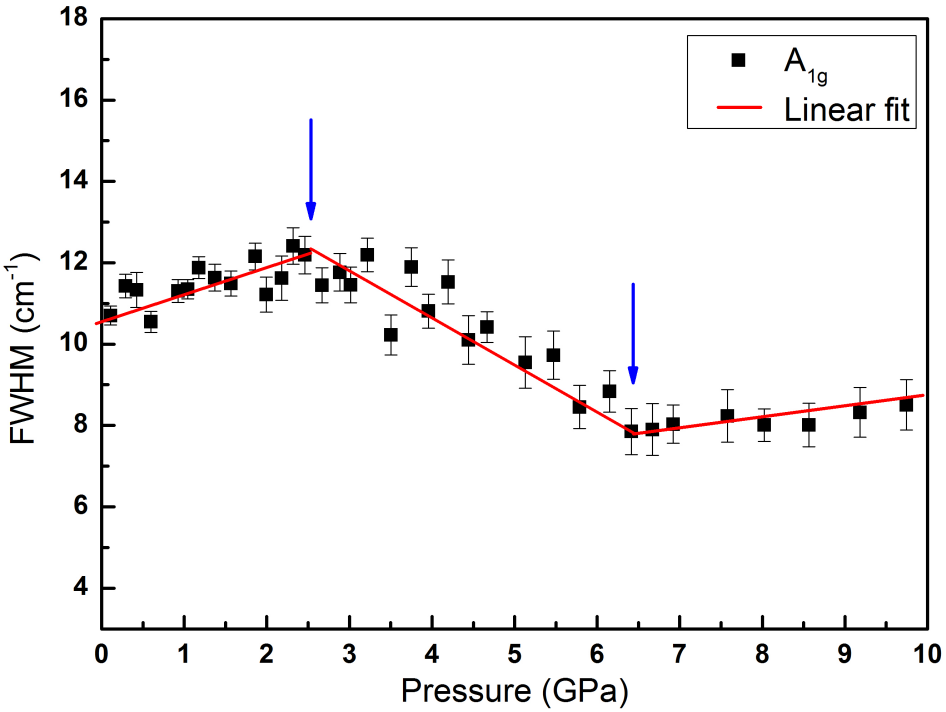

Figure 3.10. Pressure dependence of FWHM of A_{1g} mode for $TiSe_2$. The solid red lines shows the linear fit of the points. Arrows at ~2.5 GPa, and ~ 6.3 GPa indicate the isostructural electronic transitions.

Generally, Raman linewidth is inversely proportional to the lifetime of the phonon modes in a crystal. Thus, the linewidth is expected to increase with the increase of pressure. FWHM of A_{1g} mode is fitted using linear equation in three different regions as shown in the figure. Apparently, two anomalies are noted ~ 2.5 GPa and ~ 6.3 GPa. We can also note here that, there was an anomaly ~ 6 GPa in the peak position as well. The figure shows an increase in line width till the pressure ~ 2.5 GPa, then a decrease till ~ 6.3 GPa and a further increase till the structural transition. The observed evidence of unusual electron-phonon coupling ~2.5 GPa and ~6.3 GPa are clearly consistent with the theoretical predictions by Zhu et al [15] of the isostructural ($P\bar{3}m1$) TQPT. This can possibly be originated from electronic state modulation under pressure. The obtained

experimental pressure transition points are tabulated against the theoretical values in Table 3.1. The mismatch in the theoretically predicted pressures of band inversion with the experimental can be because of the approximations in calculations.

	Ambient	First band inversion	Second band inversion
Theoretical: Method 1	0 ($Z_2 = 0$)	2.75 ($Z_2 = 1$)	3.25 ($Z_2 = 0$)
Theoretical: Method 2	0 ($Z_2 = 0$)	2.75 ($Z_2 = 1$)	4.25 ($Z_2 = 0$)
Experimental	0 ($Z_2 = 0$)	2.53 ($Z_2 = 0$)	6.3 ($Z_2 = 0$)

Table 3.1. The pressure transition points of TQPT obtained from theoretical and experimental methods

3.4 Conclusions

The signature of multiple isostructural (in 1*T* phase) electronic transition was observed experimentally from Raman spectroscopic measurements of $TiSe_2$. The isostructural anomalies at ~2.53 GPa and ~6 GPa observed in linewidth is agreeing well with the first principle calculations that motivated this work. So that, these anomalies mark the trivial to non-trivial and non-trivial to trivial TQPT as a consequence of the predicted band inversion at Γ-point. A structural phase transition is also evident from the evolution of Raman spectra and formation of new peaks. The 1T phase ($P\bar{3}m1$) is expected to coexist with another phase from ~ 11GPa. The new structure has to be identified using high-pressure X-ray diffraction studies and the TQPT can be further confirmed using quantum oscillation measurement under pressure.

3.5 Bibliography

1. Kane, C. L., and E. J. Mele, *Phys. Rev. Lett.* **95**, 226801 (2005).
2. Kane, C. L., and E. J. Mele, *Phys. Rev. Lett.* **95**, 146802 (2005).
3. L.Fu, C. L. Kane, and E. J. Mele, *Phys. Rev. Lett.* **98**,106803 (2007).
4. J. E.Moore, and L. Balents, *Phys. Rev. B* **75**, 121306R(2007).
5. M. Z. Hassan and C. L. Kane, *Rev. Mod. Phys.* **82**, 3045 (2010).
6. M. S. Bahramy, B. J. Yang, R. Arita, and N. Nagaosa, *Nat.Commun.* **3**, 679 (2012).
7. W. Liu, X. Peng, C. Tang, L. Sun, K. Zhang, and J. Zhong, *Phys. Rev. B* **84**, 245105 (2011).
8. W. Li, X. Y. Wei, J. X. Zhu, C. S. Ting, and Y. Chen, *Phys. Rev. B* **89**, 035101 (2014).
9. S. Y. Xu et al., *Science* **332**, 560 (2011).
10. T. Sato et al., *Nat. Phys.* **7**, 840 (2011).
11. X. Xi et al., *Phys. Rev. Lett.* **111**, 155701 (2013).
12. A. Ohmura et al., *Phys. Rev. B* **95**, 125203 (2017).
13. A. Bera et al., *Phys. Rev. Lett.* **110**, 107401 (2013).
14. V. Rjaji et al., *Phys. Rev. B* **97**, 085107 (2018)
15. Z. Zhu, Y. Cheng and U. Schwingenschlogl, *Scientific Reports* **4**, 4025 (2014)
16. Yu. S. Ponosov, T. V. Kuznetsova, O. E. Tereshchenko, K. A. Kokh, and E. V. Chulkov, *JETP Lett.* **98**, 557 (2013).
17. P. P. Kong et al., *Sci. Rep.* **4**, 6679 (2014).
18. K. Saha, K. Légaré, and I. Garate, *Phys. Rev. Lett.* **115**, 176405 (2015).

19. S. Sugai, *Phys. Stat. Solidi* **129**, 13 (1985).

20. S.S. Jaswal, *Phys. Rev. B* **20** 5297(1979).

21. D. B. Lioi, D. J. Gosztola, G. P. Wiederrecht,2and G. Karapetrov, *Appl. Phys. Lett*. **110**, 081901 (2017).

22. K. Nagata, K. Ishibashi and Y. Miyamoto, *Jpn. J. Appl. Phys.* **20** 463(1981).

23. R. Vilaplana et al., *Phys. Rev. B* **84**, 184110 (2011).

24. Cardona, *High Pressure Res.* **24**, 17 (2004).

25. Y. A. Sorb et al., *J. Phys. Condens.Matter* **28**, 015602 (2016).

26. V. Rajaji et al., *Appl. Phys. Lett.* **109**, 171903 (2016).

27. S. Klotz, J. C. Chervin, P. Munsch, and G. L. Marchand, *J. Phys. D: Appl. Phys.* **42**, 075413 (2009).

Chapter 4

Raman Studies Nb Doped $Eu_{0.3}Ba_{0.7}TiO_3$

Our contribution in this work is to perform the Raman measurements on $Eu_{1-x}Ba_xTiO_3$ and Nb doped $Eu_{0.3}Ba_{0.7}TiO_3$ at ambient, lower and higher temperatures and analysis of the data. The sample preparation was done by Dr. K.M.Ruby, Dr. Chorng Haur and Dr. Ramanathan Mahendiran and have performed electrical magnetic and structural characterizations. Those data is included in the PhD thesis of Dr.K.M.Ruby.

4.1 Introduction

Transition metal oxides are a class of materials with fascinating physical properties due to the electron correlations that restrict the number of electrons at a lattice site and cause coupling among the charge, spin and orbital degrees of freedom. This gives rise to a variety of phenomena such as metal-insulator transition, superconductivity, and multiferroicity. The coexistence of more than one ferroic properties like ferroelectricity and ferromagnetism is entitled multiferroicity. The existence of multiferroicity in transition metal oxides makes these materials more compelling towards device applications such as electronic memory storage and magnetic field sensors.

4.1.1 Perovskites

Perovskite oxides are one of the most extensively studied, technologically useful class of materials [1]. It has ABO_3 chemical formula where A and B are cations with different ionic radii and these two sites can accommodate almost every element in the periodic table [2]. This exceptional ‘hospitality' of the perovskite structure give rise to a huge range of properties, like ferroelectricity, ferromagnetism, colossal magnetoresistance, piezoelectricity, multiferroicity, and metal−insulator transitions [3-6]. The major reason for this remarkable characteristic of perovskites is the instability of its cubic structures which leads to structural distortions that lower the energy. Hence, these materials usually have rich structural phase diagrams. [7]

In ABO_3 structure, the B-site cation occupies the body center position with oxygen octahedra around, as BO_6, whereas A-site cation occupies a corner position. The A, B, and O

sites are coordinated to 12, 6, and 8 atomic sites, respectively. The most common distortions in perovskites are off-centering of the B-site cation (those that give rise to ferroelectricity) and tilts or rotations of the BO_6 octahedra, as shown in Figure 4.1 [8]. There are some well-known perovskites like $BaTiO_3$ and $PbTiO_3$ that show polar and ferroelectric nature in low symmetry structures. But, most of the perovskites show octahedral rotations and tend not to be polar. Octahedral distortions optimize the A-site cation coordination environment whereas ferroelectric distortions are the result of the B-site bonding preferences [9,10].

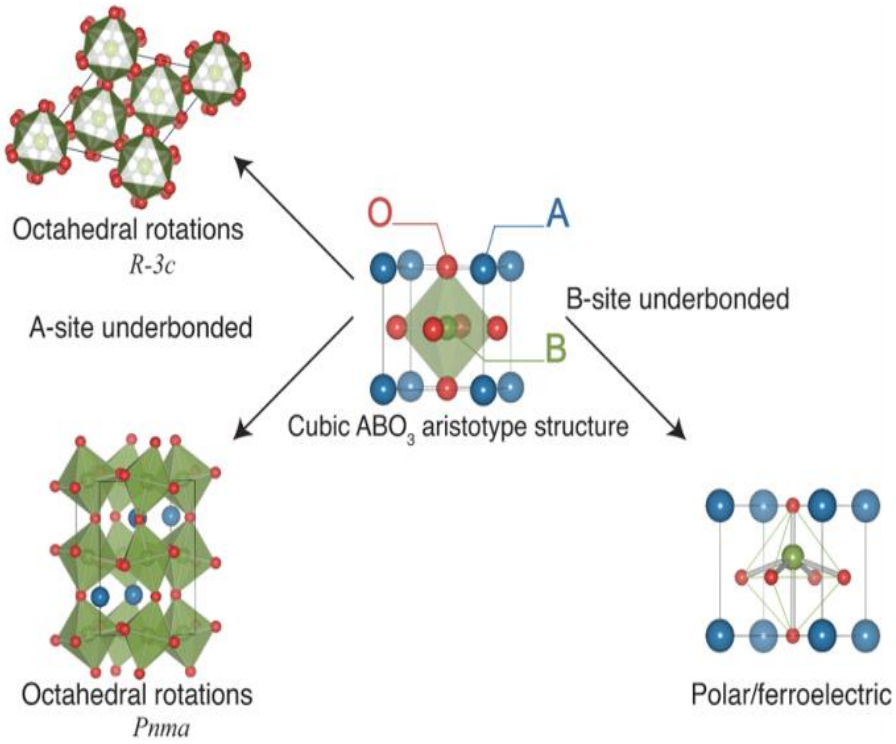

Figure 4.1. Adapted with permission from (J. Phys. Chem. C 117, 26, 13339-13349). Copyright(2013) American Chemical Society.

4.1.2 Europium doping in $BaTiO_3$

Europium Titanate ($EuTiO_3$) and Barium titanate ($BaTiO_3$) are perovskites with Ti^{4+} cations in the B perovskite site. $BaTiO_3$ is a widely used perovskite-type ferroelectric which undergoes several structural transitions (at ambient pressure); from cubic ($Pm\bar{3}m$) to tetragonal (*P4mm*) at 403K, from tetragonal (*P4mm*) to orthorhombic (*Amm2*) at 278K, and from orthorhombic (*Amm2)* to rhombohedral (*R3m*) at 188K, with decreasing temperature. All the low-temperature phases are ferroelectric and only the high-temperature cubic phase is paraelectric [11]. $EuTiO_3$ adopts the cubic perovskite structure similar to that of $BaTiO_3$ ($Pm\bar{3}m$) at room temperature and have a structural transition to the tetragonal (*I4/mcm*) on cooling below room temperature [12]. While $BaTiO_3$ is non-magnetic and ferroelectric at room temperature $EuTiO_3$ is antiferromagnetic and quantum paraelectric. Hence, the emergence of ferroelectricity with increasing Ba content in $EuTiO_3$ will be interesting. The electrical transport measurements and magnetization measurements by our collaborators show exotic properties in these compounds. In the first part of this chapter, we are trying to explain the structural origins of ferroelectric transition of these compounds using Raman spectroscopy.

4.1.3 Nb doped $Eu_{1-x}Ba_xTiO_3$

Ferroelectricity and metallicity were considered impossible to coexist as the static internal fields that cause the emergence of ferroelectricity will be screened by conduction electrons in metals. But in 1965, Anderson and Blount predicted the possibility of a ferroelectric metal, in which a ferroelectric-like structural transition occurs in the metallic state [13]. Recently, there are reported evidence of metallic conductivity in $BaTiO_3$

formed by carrier electron doping and by introducing oxygen vacancies [14-17]. This proves that the presence of itinerant electrons does not suppress the ferroelectric phase instantly. Instead, the ferroelectric distortion is sustained even under metallic conductivity [18]. Nb^{5+} doped $Eu_{1-x}Ba_xTiO_3$ is expected to show this nature. Thus electrical transport and magnetization experiments are conducted. The second the part of this work, Nb^{5+} is doped in different concentrations in the ferroelectric material and the effect is observed using Raman spectroscopy to support those measurements.

4.2 Experimental Details

Polycrystalline $Eu_{1-x}Ba_xTiO_3$ samples are synthesized through solid-state reaction method by mixing required the stoichiometric proportion of Eu_2O_3, $BaCO_3$ and TiO_2 powder then grinding it and sintering at 1200° C for 24 hours in 95% Ar and 5 % H_2 atmosphere. Powders were pressed in a uniaxial press to form pellets and these pellets were sintered at 1300° C for 24 hours after two intermediate grinding and annealing at 1200° C. Nb doped samples were prepared from high purity (99.99%) $BaCO_3$, Eu_2O_3, TiO_2, Nb_2O_5 powders. Pellets of stoichiometric amounts of the starting materials were calcined at 1100^0C for 20 h in flowing H_2, with a second regrinding or repelletization at 1350^0C for 20 h (again in flowing H_2). Powder X-ray diffraction (XRD) using CuKα radiation was performed at room temperature to examine the phase and crystal structure of the samples.

The Raman scattering measurements were performed in backscattering geometry using a custom-built Raman spectrometer (as described in the experimental section in

chapter 2) with a laser excitation of 532 nm using a frequency-doubled Nd-YAG laser. A laser power of 0.5 mW was used at the sample. Temperature-dependent Raman measurements were carried out from 100 K to 300 ± 1 K using Linkam stage (LHS 600).

4.3 Results and Discussion

Raman spectra of $Eu_{0.1}Ba_{0.9}TiO_3$ is given in Figure 4.2 for a spectral range 200 cm^{-1} to 800 cm^{-1}. We see two broad bands similar to that of the Raman spectra of $BaTiO_3$. $BaTiO_3$ exhibits many unusual features in its Raman spectra such as the broad and asymmetric bands peaked at about 265 cm^{-1} and 520 cm^{-1} and a sharp dip at 186cm^{-1}. These features persist even in its cubic phase ($Pm\bar{3}m$) where all optical phonons should be Raman inactive. This interesting behavior has been quantitatively understood based on the phonon-phonon coupling of three A_1(TO) modes via anharmonic interactions [19]. These A_1(TO) phonons modes have only diagonal Raman polarizability components $\alpha_{xx} = \alpha_{yy}$ (which has contributions to A_1 and B_1 phonons) and α_{zz} (the component which involves only A_1 phonons) which persist in the cubic phase due to disorder in the position of Ti^{4+} ions in the unit cell [20]. This kind of coupling is a characteristic found in modes which have a large spread of frequency. In the case of coupled oscillators fitting using real coupling between the modes, the frequency parameters may not have physical meaning by itself [21]. The peak at 310 cm^{-1} is assigned to the E + B_1 mode which has a non-vanishing Raman polarizability component α_{xz} for the x-polarized phonon and α_{yz} for the y-polarized phonon in the tetragonal phase. Raman spectra of $Eu_{0.1}Ba_{0.9}TiO_3$ which looks similar to that of $BaTiO_3$ encourages us to use the same model to study the system.

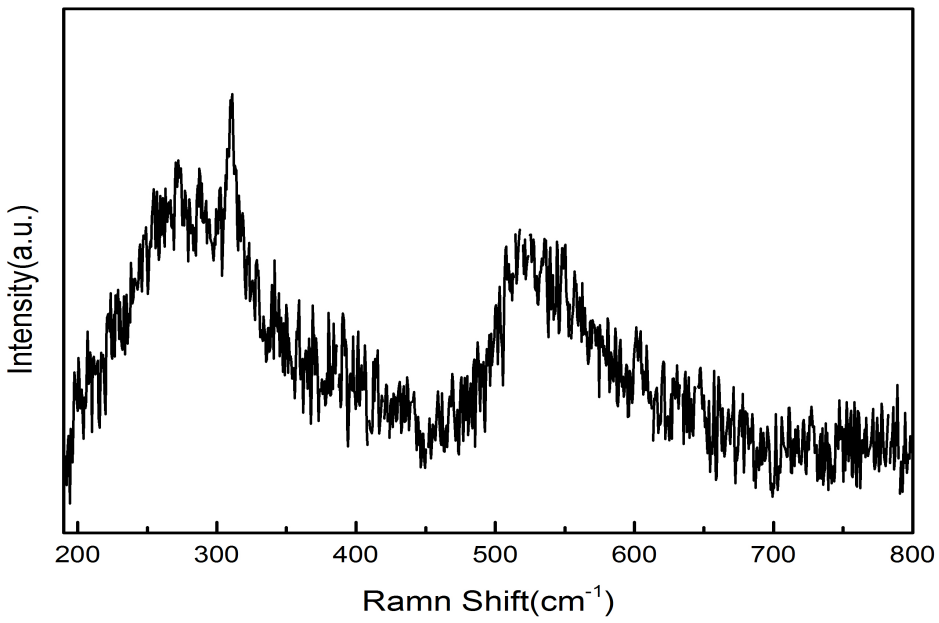

Figure 4.2. Raman spectra of $Eu_{0.1}Ba_{0.9}TiO_3$

In this model of three coupled oscillators, the Stokes Raman line shape is given by

$$I(\omega) = A[n(\omega) + 1]\ \mathrm{Im}\ [T^{\dagger}GT] \tag{4.1}$$

where $T = [T_1, T_2, T_3]$ is the vector that incorporates the Raman scattering amplitudes G is understood from the equation in which the inverse matrix function is given as,

$$G^{-1}(\omega) = \Omega^2 - \omega^2 I - i\omega\Gamma \tag{4.2}$$

Here $I = \{\delta_{ij}\}$ is the unit matrix and Ω^2 **(**Γ**)** is the force constant matrix described as,

$$\Omega^2 = \begin{pmatrix} \omega_1^2\ \omega_{12}^2 & 0 \\ \omega_{12}^2\ \omega_2^2\ \omega_{23}^2 \\ 0 & \omega_{23}^2\ \omega_3^2 \end{pmatrix} \tag{4.3}$$

$$\Gamma = \begin{pmatrix} \Gamma_1 & 0 & 0 \\ 0 & \Gamma_2 & 0 \\ 0 & 0 & \Gamma_3 \end{pmatrix} \tag{4.4}$$

And, ω_1, ω_2, and ω_3 are the uncoupled mode frequencies ω_{12} and ω_{23} are the strength of coupling between modes 1 and 2 and modes 2 and 3 respectively. Also, ω_{13} is taken as 0 as there is no spectral overlap of the first and the third modes. [n(ω) +1] is the usual Bose-Einstein factor and A is a constant. The calculated I(ω) has been least-squares fitted to the experimental data(background subtracted) in the range of 200—700 cm using Matlab with eight fitting parameters ω_1, ω_2, ω_3, Γ_1, Γ_2, Γ_3, ω_{12}, and ω_{23}.

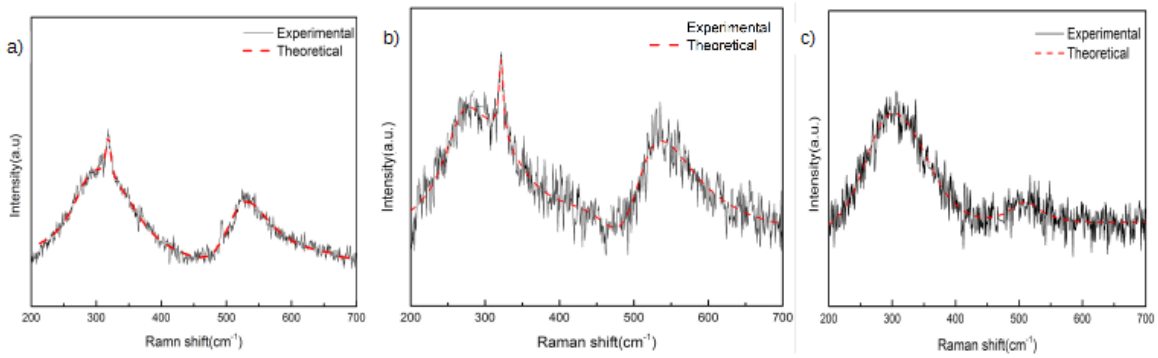

Figure 4.3. Raman spectra of a)$Eu_{0.1}Ba_{0.9}TiO_3$ b) $Eu_{0.2}Ba_{0.8}TiO_3$ and c) $Eu_{0.1}Ba_{0.7}TiO_3$

The fitted data for various different doping of Eu in $BaTiO_3$ is shown in the Figure 4.3. The fitted parameters thus obtained for all the three compositions are given in the Table 4.1. There is not much information that can be gathered from these values. But the clear effect that is seen with doping is the disappearance of B_1 mode (B_1 mode is fitted separately using Lorentzian peak) which is the characteristic tetragonal peak seen in $BaTiO_3$ as well.

	Γ_1	Γ_2	Γ_3	ω_1	ω_{12}	ω_2	ω_{23}	ω_3
$Eu_{0.1}Ba_{0.9}TiO_3$	0.9	69	7.5	186.7	143.8	326.5	307.2	472.3
$Eu_{0.2}Ba_{0.9}TiO_3$	0.9	71	7.4	188.7	143.7	326.5	305.1	471.9
$Eu_{0.3}Ba_{0.7}TiO_3$	0.8	72	7.2	190.5	143.4	326..5	303.4	472.0

Table 4.1. Fitting parameters obtained by least squre fitting of intensity for $Eu_{0.1}Ba_{0.9}TiO_3$, $Eu_{0.2}Ba_{0.8}TiO_3$ and $Eu_{0.1}Ba_{0.7}TiO_3$.

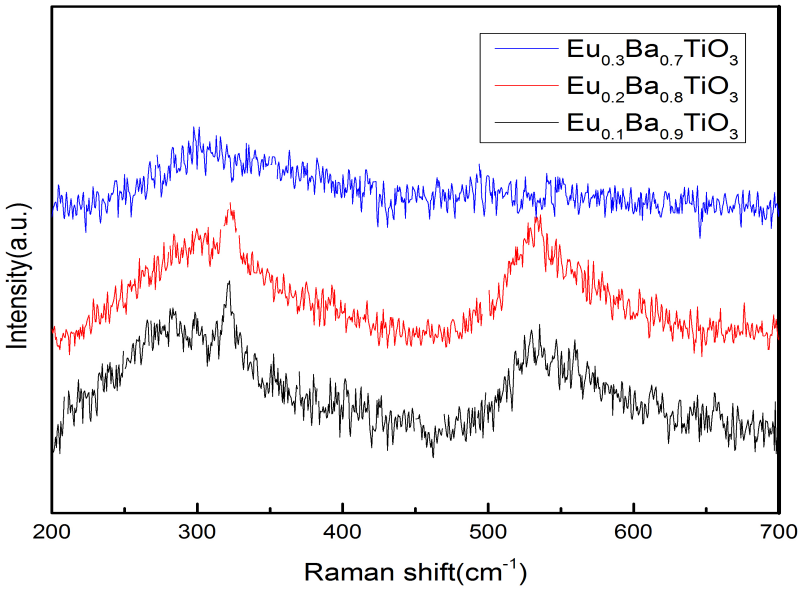

Figure 4.4. Stack plot of Raman spectra of $Eu_{1-x}Ba_xTiO_3$ (x=0.7,0.8,0.9)

The stack plot of $Eu_{1-x}Ba_xTiO_3$ is given in Figure 4.4 for the measurements at 301K. This gradual change from tetragonal to cubic characteristic spectra is expected with increased Eu doping, since the cubic phase of pure $EuTiO_3$ is present from near room temperature (300K) [12]. Also, the result electrical transport studies by our collaborators match really well with this assumption. The ferroelectric transition of $Eu_{0.3}Ba_{0.7}TiO_3$ is observed near room temperature which is clear from its phase diagram shown in the Figure 4.5.

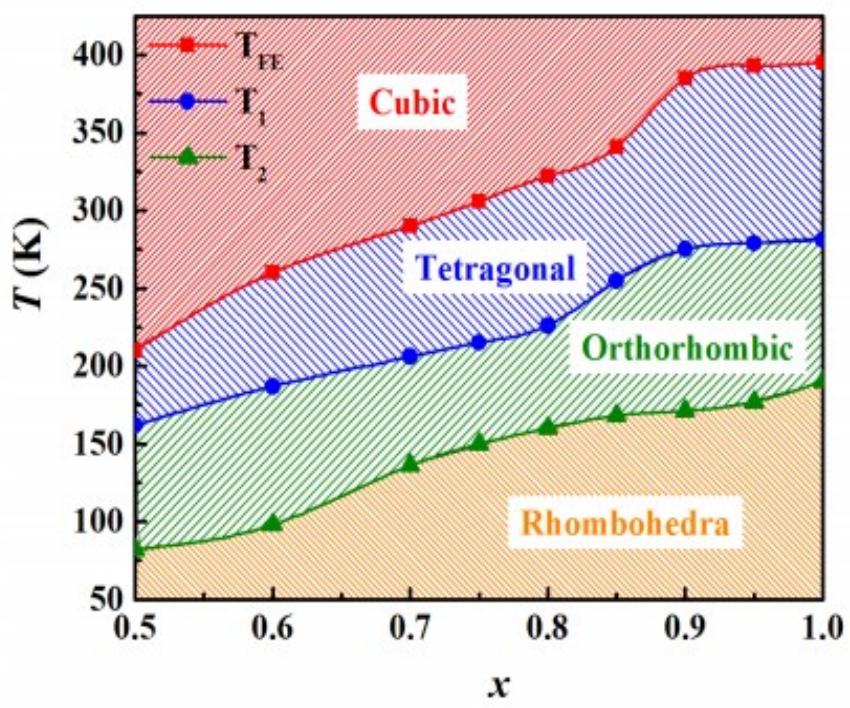

Figure 4.5. The phase transition temperatures T_{FE} (Cubic to tetragonal or paraelectric to ferroelectric transition), T_1 (Tetragonal to Orthorhombic) and T_2 (Orthorhombic to Rhombohedral) as a function of x for $Eu_{1-x}Ba_xTiO_3$. Shaded areas represent different phases.

To understand more about the structural phase transition of $Eu_{0.3}Ba_{0.7}TiO_3$ temperature depended studies have been done from 302 K to 123K. The stack plot of temperature dependent measurement is shown in Figure 4.6. The characteristic tetragonal peak is observed to appear above 295K on cooling which is accompanied with the ferroelectric transition and gets sharper with decrease of temperature. But this transition does not affect the broad Raman peaks in the spectra. Hence, to get a better interpretation of phonon modes, fitting is done for all the Raman spectra at various temperature as explained in the previous section at. Figure 4.7 shows the dependence of fitting parameters to temperature.

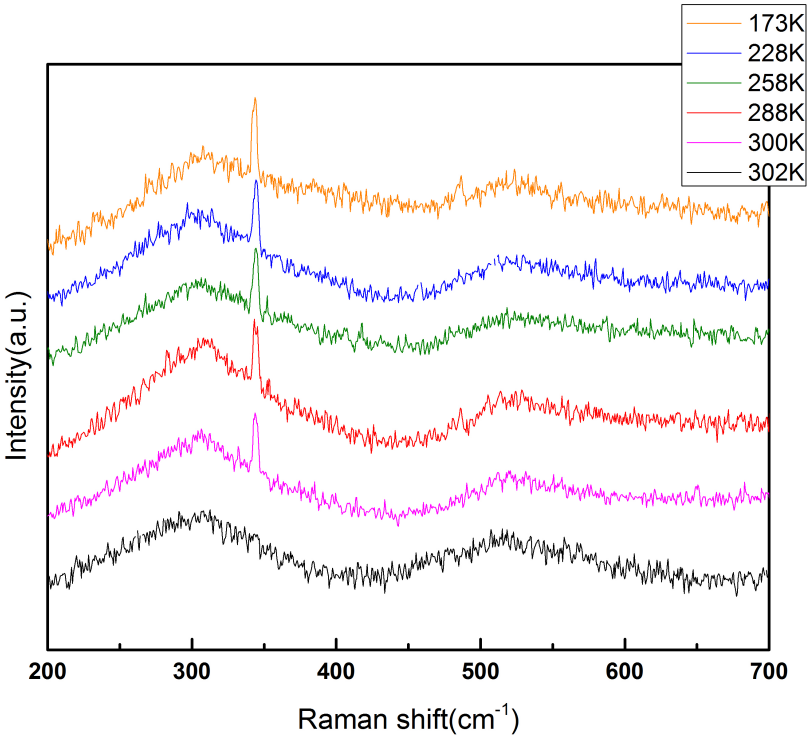

Figure 4.6. Stack plot of Raman spectra of $Eu_{0.3}Ba_{0.7}TiO_3$ at different temperatures.

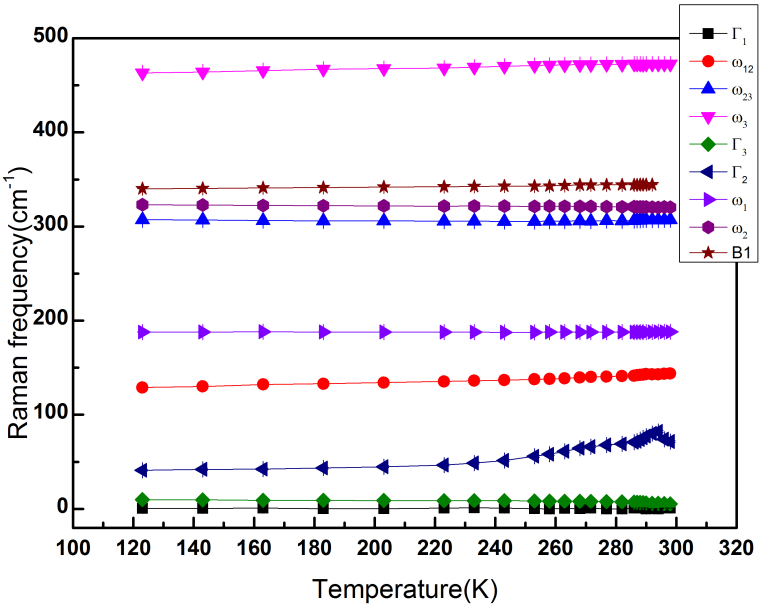

Figure 4.7.The fitted parameters of $Eu_{0.3}Ba_{0.7}TiO_3$ plotted as a function of temperature for a temperature range123K to 302K.

The following features are noteworthy from the plot.

i. From the spectra it is clear that, ω_1 and Γ_1 does not show any notable changes with temperature.

ii. The frequency ω_2 decreases with temperature and ω_3 increases similar to what is observed in $BaTiO_3$ [22].This behaviour of ω_3 is an interesting consequence of the mode coupling.

iii. The linewidth of the middle phonon mode, Γ_2 shows a maximum at 294K just before the structural transition as shown in Figure 4.8. The linewidth has become almost double from ~ 41 cm^{-1} at 123K to ~ 82 cm^{-1} at 294K. This effect is also similar to the linewidth anomaly in $BaTiO_3$ [22] and has been considered as the effect of disorder. That is, the Ti^{4+} ions sit off-center in the unit cell and tunnel through a double well in the direction of the ferroelectric axis [23].

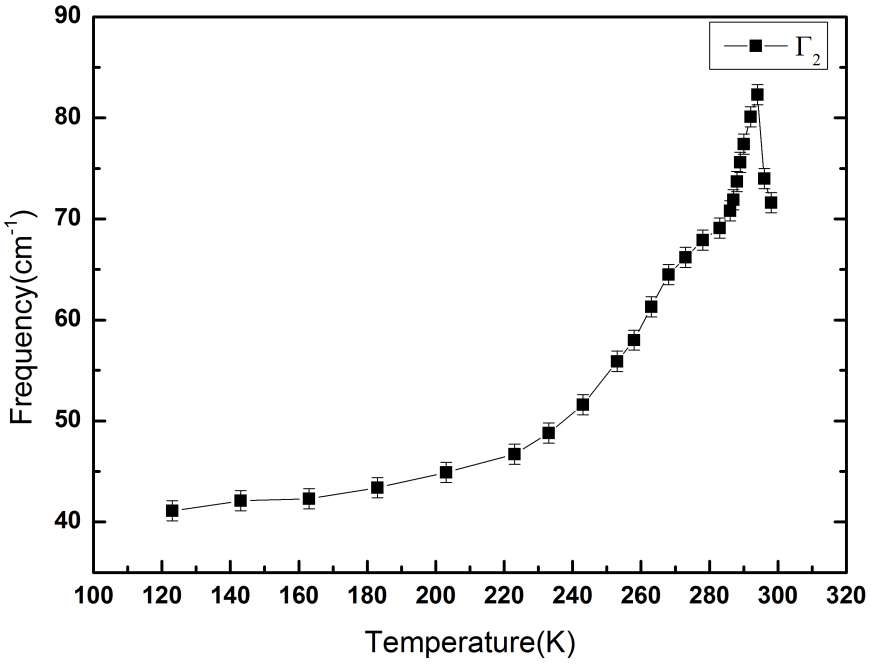

Figure 4.8. Plot of fitting parameter Γ_2 with respect to increasing temperature.

iv. The coupling parameters ω_{12} and ω_{23} show a noticeable change near 253K shown in Figure 4.9*a* and 4.9*b* respectively which may be representing the structural transition from tetragonal to orthorhombic phase. But the transition temperature does not match closely with the temperature obtained from the electrical measurements. This may be because the structural transition does not occur suddenly by entirely changing the bulk properties that comes out in transport measurements, but goes through a mixed phase. However, these parameters does not show a visible change near the ferroelectric transition temperature.

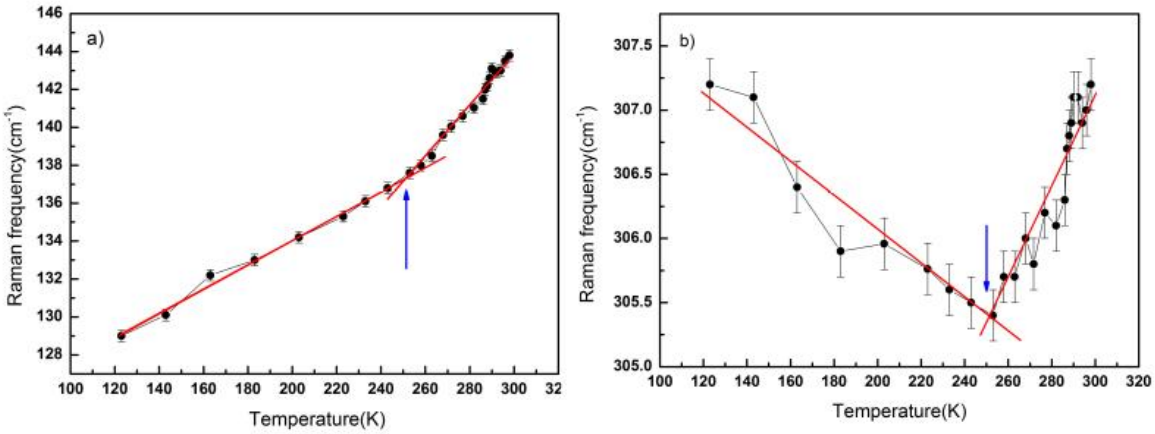

Figure 4.9. Plot of coupling a) ω_{12} and b) ω_{23} parameters with respect to increasing temperature

Small substitutions of Nb^{5+} for Ti^{4+} in the perovskite $EuTiO_3$ give rise to metallic behaviour [24] while in case of $BaTiO_3$ on Nb substitution is semiconducting up to at least 20% substitution [25]. In our work, we have seen that the substitution of Nb in the Ti site of $Eu_{0.3}Ba_{0.7}TiO_3$ shows metallic character even at very small substitution from electrical transport studies. An important question is what microstructural changes happen when charge carriers are introduced into a ferroelectric material. In $BaTiO_3$ some studies

indicate that ferroelectricity and metallic behavior may coexist [26,27], while others have suggested that they only do so in separated region [28]. To sort out this controversy, we have done Raman spectroscopy of various compounds with different percentages of Nb substitution (1 %, 3%, 5% and 10%) in $Eu_{0.3}Ba_{0.7}TiO_3$ and tried to picturise the mechanism of this metallic nature from a molecular point of view.

Figure 4.10 is the stack plot of Nb substituted $Eu_{0.3}Ba_{0.7}TiO_3$ in various composition at 299K (below the ferroelectric transition of parent compound) after background subtraction. The effects that are seen from the plot with increasing doping percentage are; i) the spectra is getting weaker, ii) the coupled-phonon peaks are getting more broader, and iii) the characteristic tetragonal peak is disappearing with doping. The spectra of 10% Nb substituted $Eu_{0.3}Ba_{0.7}TiO_3$ look very much like the paraelectric cubic phase of $Eu_{0.3}Ba_{0.7}TiO_3$.

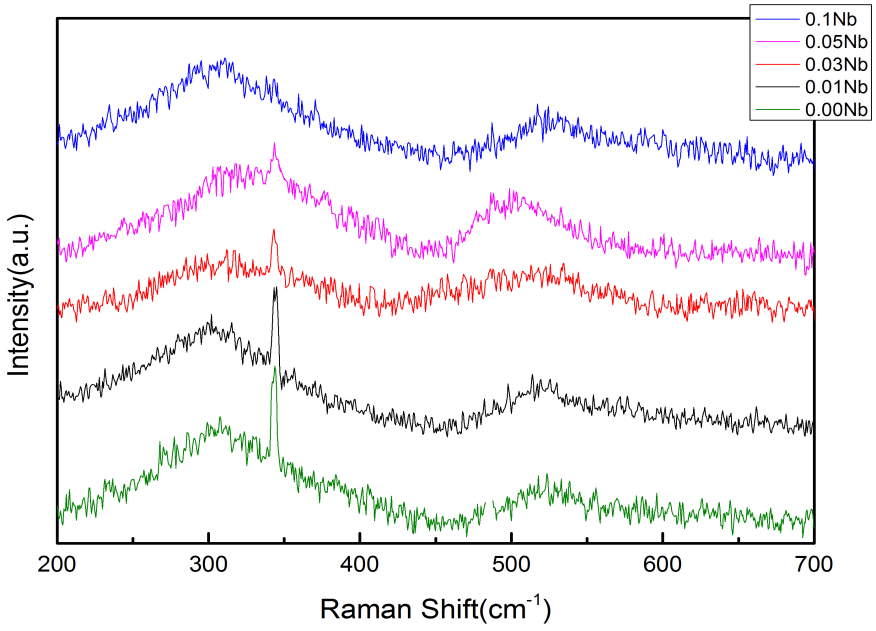

Figure 4.10. Stack plot of $Eu_{0.3}Ba_{0.7}TiO_3$ substituted with different concentration of Nb.

Off-centering of the Ti ion with respect to the oxygen octahedron is the source of the local polarization. The deformations in BO_6 octahedra that increases along with doping, make the crystal to lose the polar nature and hence the 310 cm^{-1} peak is broadening and disappearing gradually. In case of 10% Nb substituted $Eu_{0.3}Ba_{0.7}TiO_3$, B_1 mode is missing from the spectra at many points. But, there are a few points where the spectra (especially the second broad peak) are smeared, and the B_1 peak is still visible. For a comparison, both the spectra is shown in the Figure 4.11. This means that local structure of can have ferroelectric domains regardless of its long-range average crystal symmetry (X-Ray Diffraction shows cubic structure).

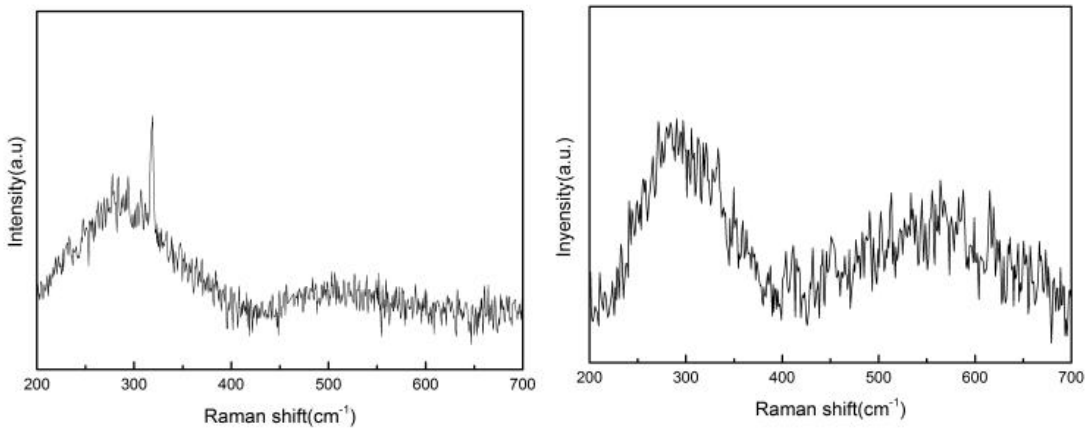

Figure 4.11. The two different types of spectra obtained for 10% Nb substituted $Eu_{0.3}Ba_{0.7}TiO_3$ at different points on the sample.

To understand more about the effect of Nb substitution, fitting has been done for each spectrum in the same method as before. The fitting parameters thus obtained are given in Table 4.2. There is a sudden change visible in ω_1 and ω_{12} when the doping percent change from 0 to 1. Afterwards, the change in these values appears gradual with doping. This is consistent with the transport measurements where there is a sudden

reduction in resistivity with 1% Nb doping. The introduction of random potentials by Nb substitution on the Ti site result in the suppression of dipole-dipole correlations which can be the reason for this change in the values of ω_1 and ω_{12}.

Nb substitution percentage	Γ_1	Γ_2	Γ_3	ω_1	ω_{12}	ω_2	ω_{23}	ω_3
0%	0.8	72	7.2	190.5	143.4	326..5	303.4	472.0
1%	0.8	70	7.7	187.3	146.7	326.5	304.1	472.0
3%	0.9	69	8.5	186.1	148.9	326.5	304.2	471.6
5%	0.9	68	9.4	186.5	149.9	326.4	304.1	471.5
10%	0.8	66	10.4	184.6	151.3	326.7	304.4	472.3

Table 4.2. Fitting parameters obtained for different percentage of Nb substituted in $Eu_{0.3}Ba_{0.7}TiO_3$

Temperature dependent measurements are done for all these samples to understand the evolution of structural transition with doping. The tetragonal to cubic transition with increasing temperature is marked by sudden change in the Γ_2 value (as seen in the case of parent compound) and the disappearance of B_1 peak. The stack plot of both the parameters for different compositions is shown in the Figure 4.12 and 4.13. In the case of 10% Nb substituted $Eu_{0.3}Ba_{0.7}TiO_3$ the B_1 mode is not present in any temperature. Thus we depend solely on Γ_2 value to understand the structural transition in that case.

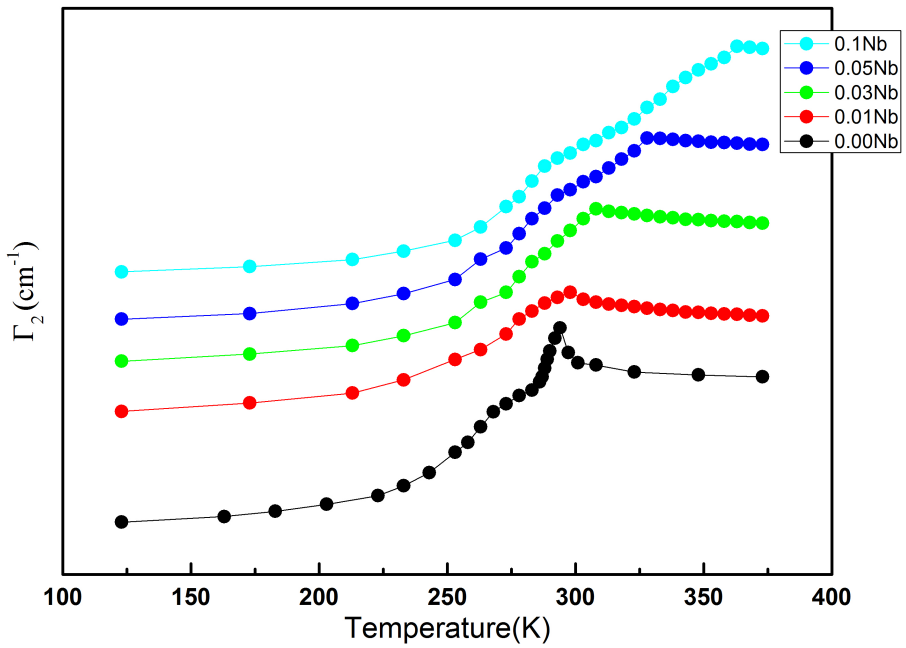

Figure 4.12. Stack plot of change in Γ_2 values with temperature for different percentage of Nb substituted in $Eu_{0.3}Ba_{0.7}TiO_3$.

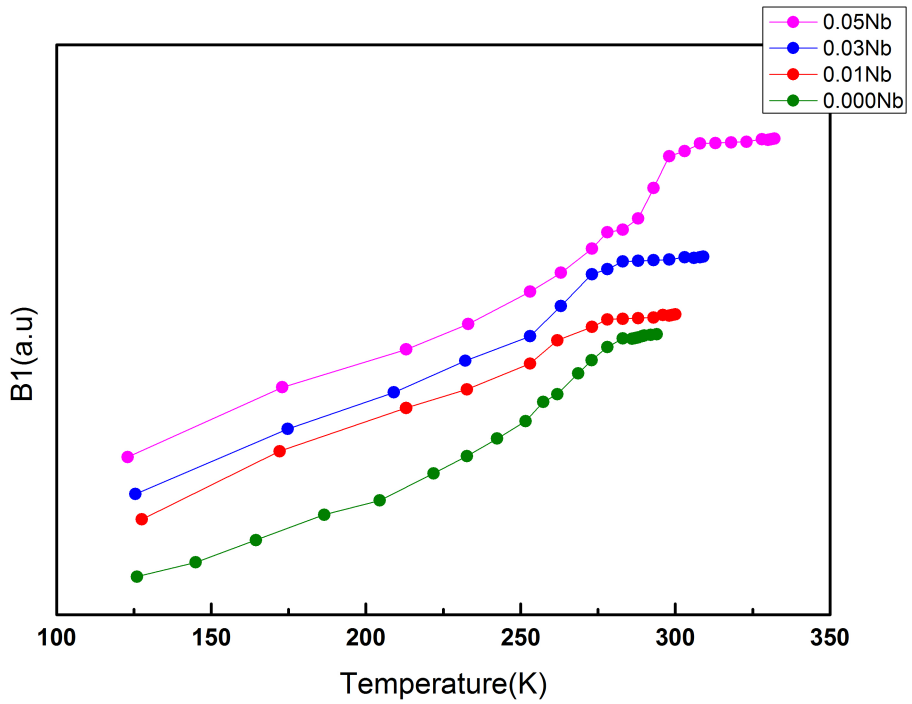

Figure 4.13. Stack plot of change in B1 peak position with temperature for different percentage of Nb substituted in $Eu_{0.3}Ba_{0.7}TiO_3$.

The transition temperature values thus obtained from both the plots are shown in Figure 4.14. The temperature value from both the plots closely matches confirming the ferroelectic to paraelectric or tetragonal to cubic transition. The transition temperature is shifted to higher temperatures with increasing Nb substitution. This is similar to the Nb doping behavior observed in pure $EuTiO_3$ [24]. The sharp change in Γ_2 value at the transition becomes more smeared with increasing doping.

The evidences from XRD and electrical transport measuremnts shows that charge carriers screen the long-range electrostatic interactions responsible for ferroelectric order. However, from Raman studies we can understand that there are local ferroelectric domains persisting in the crystal even after 10% doping. This nature of the system can lead to the phenomenon of metallic ferroelectricity.

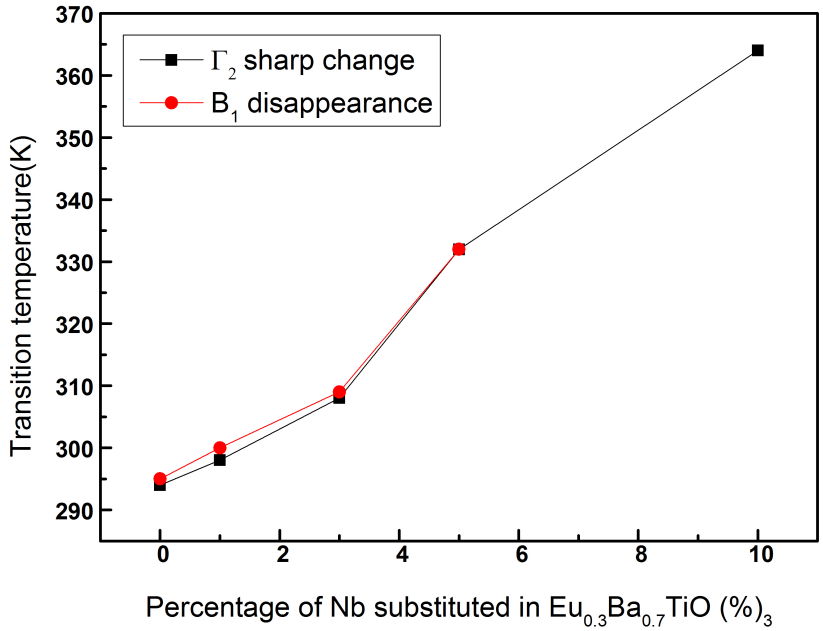

Figure 4.14. Transition temperature values obtained from sharp change in Γ_2 and B_1 disappearance for different percentage of Nb substituted in $Eu_{0.3}Ba_{0.7}TiO_3$.

4.4 Conclusion

In this thesis, we have tried to understand the structural and microscopic origins of ferroelectric properties in $Eu_xBa_{(1-x)}TiO_3$ (x = 0.1,0.2 and 0.3) and to understand the metallicity that gets introduced in the system immediately when Nb is substituted replacing Ti in the $Eu_{0.3}Ba_{0.7}TiO_3$. We observe that the ferroelectricity in $Eu_xBa_{(1-x)}TiO_3$ mimics the nature of $BaTiO_3$. The tetragonal to cubic transition in $Eu_{0.3}Ba_{0.7}TiO_3$ takes place ~ 295K which matches with the observed transport properties and ferroelectric to paraelectric transition temperature. Nb doping in the sample introduces deformations in the Ti/Nb-O_6 octahedra that increases along with doping make the crystal to lose the polar nature and hence appears cubic and metallic in X-ray diffraction and transport studies respectively. But Raman being a local probe can see a different effect from its bulk properties. That is, even though a long-range ordering of dipoles which results in the ferroelectric behavior of the crystal is suppressed as a whole, there are ferroelectric domains continue to exist in the crystal even after 10% doping which shows the effect of smeared ferroelectric nature in the Raman spectra. Thus it is a system which is competent enough to show the exciting phenomenon of metallic ferroelectricity.

4.5 Bibliography

1. O. Muller and R. Roy, *Crystal Chemistry of Non-Metallic Materials* (Springer-Verlag, New York, 1974)
2. D.G. Schlom, L.Q. Chen et al., *J. Am. Ceram. Soc*. **91**, 2429 (2008)
3. J.G. Bednorz, K.A. Müller,*Zeitschrift für Physik B Condensed Matter* **64,**189 (1986)

4. R. Mahendiran, R. Mahesh, A.K. Raychaudhuri and C.N.R. Rao, *J. Phy. D- Appl. Phy.* **28**, 1743 (1995)
5. A. Urushibara et al., P*hysical Review B*, **51** 14103 (1995)
6. Y. Tokura et al., *Journal of the Physical Society of Japan* **63**,3931 (1994)
7. K. M. Rabe, Ph. Ghosez, *Physics of Ferroelectrics: A Modern Perspective* (Springer-Verlag, New York, 2007)
8. N. A. Benedek and C. J. Fennie, *J. Phys. Chem. C* **117**,13339 (2013)
9. P. M. Woodward, *Acta Crystallogr*. **B53**, 44 (1997)
10. M. W. Lufaso, P. M. Woodward, *Acta Crystallogr*. **B57**, 725(2001)
11. W. Han et al., *J. Appl. Phy.* **113**, 193513 (2013)
12. V.Goian et al., *Phy. Rev B* **86**, 054112 (2012)
13. P. W. Anderson, and E. I. Blount, *Phys. Rev. Lett.* **14**, 217(1965).
14. J. F. Marucco, M. Ocio, A. Forget, and D. Colson, *J. Alloys Compd.* **262**, 454 (1997).
15. K. Page, T. Kolodiazhnyi, T. Proffen, A. K. Cheetham, and R. Seshadri, *Phys. Rev. Lett.* **101**, 205502 (2008)
16. T. Kolodiazhnyi, M. Tachibana, H. Kawaji, J. Hwang, and E. Takayama-Muromachi, *Phys. Rev. Lett.* **104**, 147602 (2010).
17. J. Hwang, T. Kolodiazhnyi, J. Yang, and M. Couillard, *Phys. Rev. B* **82**, 214109 (2010)
18. Y. Iwazaki, T. Suzuki, Y. Mizuno and S. Tsuneyuki, *Phys. Rev. B* **86**, 214103 (2012)
19. A. Chaves, R.S. Katiyar, and S.P.S. Porto, *Phys. Rev. B* **10**, 3522 (1974).
20. A. K. Sood, N. Chandrabhas, D. V. S. Muthu, and A. Jayaraman, *Phys. Rev. B* **51**,8892 (1995)
21. J. A. Sanjuro, R. S. Katiyar and S. P. S. Porto, *Phys. Rev. B* **22,** 2396 (1980)

22. A. Scalabrin, A.S. Chaves, D. S. Shim and S. P. S. Porto, *Phys. Stat. Sol. (B)* **79**, 731 (1977)

23. A. Scalabrin, S.P.S. Porto, H. Vargas, C.A.S. Lima, and L.C.M. Miranda, *Solid State Commun.* **24**, 291 (1977)

24. L. Li et al., P*hy. Rev. B* **92**, 024109 (2015).

25. K. Page, T. Kolodiazhnyi, T. Proffen, A.K.Cheetham and R.Seshadri, *Phy. Rev. Lett*. **101**, 205502 (2008).

26. Y. Wang, X. H. Liu, J. D. Burton, S. S. Jaswal, and E. Y. Tsymbal, *Phys. Rev. Lett.* **109**, 247601 (2012).

27. T. Kolodiazhnyi, M. Tachibana, H. Kawaji, J. Hwang, and E. Takayama-Muromachi, *Phys. Rev. Lett.* **104**, 147602 (2010).

28. I.K. Jeong, S. Lee, S.-Y. Jeong, C. J. Won, N. Hur, and A. Llobet, *Phys. Rev. B* **84,** 064125 (2011).